Application of LA ICP-MS sulphide analysis and methodology for deciphering elemental paragenesis and associations in addition to multi-stage processes in metamorphic gold settings

Blandine Gourcerol, Daniel J Kontak, Phillips C Thurston, Joseph A Petrus

Title: Application of LA ICP-MS sulphide analysis and methodology for deciphering elemental paragenesis and associations in addition to multi-stage processes in metamorphic gold settings

B. Gourcerol[1,2*], D.J. Kontak[1], P.C. Thurston[1], J.A. Petrus[1]

[1]Mineral Exploration Research Centre, Laurentian University, Sudbury, Ontario, Canada P3E 2C6

[1] Now BRGM (Bureau de Recherche Géologique et Minière), Orléans, France

***Corresponding author: gourcerol.blandine@gmail.com**

Abstract

Quantitative laser ablation inductively coupled plasma-mass spectrometry (LA ICP-MS) element distribution analysis represents a relatively new and powerful approach to assess gold mineralizing processes. Although there is a trend towards imaging in LA ICP-MS, this article demonstrates that the compilation of the individual time-slice datasets (TSD) from LA analyses provides greater potential to explore and better understand ore systems. Based on several analyses of gold-bearing sulphides from a variety of lode gold mineralized settings, this study introduces new diagrams and geostatistical techniques as recommended procedures to be applied to any gold deposit environment to better understand its genesis with possible exploration implications. The nature of the mineralizing fluid is investigated by studying Ni and Co variations in the sulphide grains in environments ranging from ultramafic to felsic, whereas upgrading of gold tenor within an ore deposit is identified using Au versus Ag plots grouped by element association and elemental geochemical affinity. Furthermore, the textural transformation and coupled dissolution/precipitation (CDP) in pyrite is documented using Ag versus Ni plots with associated defined fields (i.e., diagenetic versus metamorphic). Lastly, standard

geostatistical tests are used to assess element associations through agglomerative hierarchical clustering and exploratory statistical methods. Meanwhile, a multidimensional scaling approach can evaluate the geochemical affinity of the mineralizing fluids.

Keywords: laser-ablation ICP-MS, sulphides, gold, trace elements, procedure, and statistical analysis

1. Introduction

Quantitative laser ablation inductively coupled plasma-mass spectrometry (LA ICP-MS) element distribution maps and profiles of sulphides are relatively new and powerful geochemical techniques that provide important insight into the identification and interpretation of multi-dimensional element coupling and decoupling, elemental paragenesis and mineralizing events. These methods have been applied to a wide variety of gold deposit types (e.g., Large et al., 2007, 2009, 2011; Ulrich et al., 2009; Cook et al., 2013; Bull and Large, 2014; Gao et al., 2015; Lawley et al., 2015; Kontak 2015). The application to multiple gold-associated sulphide phases (e.g., diagenetic and later pyrite generations, metamorphic pyrrhotite and hydrothermal arsenopyrite) has provided concentration data and the spatial context of various elements in the host sulphide phase (e.g., primary grains, recrystallized grains, growth patterns, fracture networks, inclusions) at a multi-micron scale (i.e., 10s μm). Importantly, this method also minimizes the averaging effect of conventional bulk solution-based ICP-MS analyses, which commonly masks important information that relates to elemental associations and their paragenesis (e.g., Ulrich et al., 2009; Warren et al., 2015; Jenner and Arevalo, 2016).

Most previously published laser ablation-ICP-MS element distribution maps were created by stitching together many time-resolved traverses or spots. This approach has visual appeal, but

may not reveal subtle element associations. Alternatively, or in tandem, time-resolved traverses can be used as "time-slice datasets" (TSD) where each sweep of the MS is treated as a separate data point providing the means to evaluate relationships between elements at a much finer scale. The strenghs of this latter approach are rarely exploited, but a few recent examples of this type of data processing generated at our institution have been presented (e.g., Dostal et al., 2015; Genna and Gaboury, 2015; McDivitt, 2016; Neyedley et al., 2016; Gourcerol et al., 2016a). The advantage of this approach is that it provides a means to identify elemental correlations not readily observed from element distribution mapping, as is illustrated below, and thus enables one to establish an elemental paragenesis for the phase analyzed and thereby the mineralized system. Therefore, the latter supplements information provided by the element distribution maps. In the case of gold deposit studies, integration of those maps and TSD treatment allows one to identify the true element association of deposits which is not easily discernable solely using the conventional technique of element distribution maps or traverses.

The purpose of this article is to present and discuss a routine means of integrating the elemental distribution maps produced from LA ICP-MS analysis of sulphides with TSD in order to optimize data interpretation in the context of : 1) elemental paragenesis, 2) deposit genesis, and by extension 3) exploration. With these goals, a selection of samples from multiple deposits are used herein to demonstrate the utility of these novel methods. In addition, several elemental plots for sulphide phases are introduced (e.g., Ag versus Ni; Co versus Co/Ni; Au versus Ag) to understand and portray the complexities of gold mineralizing events and the potential influence of host stratigraphy on fluid and hence sulphide chemistry. We also use geostatistical methods (e.g., multidimensional scaling and discriminant analysis) to: 1) confirm the element associations suggested from the maps and binary element plots; 2) confirm the number of gold mineralizing

events identified with TSD; and 3) address the nature of sulphide-transporting fluids. In order to demonstrate the effectiveness of the TSD method, we use sulphide datasets gathered from several Canadian orogenic gold deposits with which we are familiar based on our previous field and petrological studies. These include the Archean banded iron formation (BIF) - hosted Meliadine (Nunavut; e.g., Lawley et al., 2015; Gourcerol et al., 2016a, b), Meadowbank (Nunavut; e.g., Janvier et al., 2015; Gourcerol et al., 2016a, b) and Musselwhite (Ontario; e.g., Oswald et al., 2015; Gao et al., 2015; Gourcerol et al., 2016a, b) deposits consisting of sulphide (i.e., arsenopyrite, pyrite and pyrrhotite, respectively) replacement of Fe-rich material (e.g., magnetite), as well as the Phanerozoic metaturbidite-hosted Beaver Dam deposit (Nova Scotia) in which sulphides such as arsenopyrite occur mainly as quartz vein filling (e.g., Kontak et al., 1993; Sangster and Smith, 2007; Kontak et al., 2013).

2. Analytical methods

2.1 LA ICP-MS sulphide trace element chemistry

The trace element chemistry of several sulphides were determined by LA ICP-MS in Laurentian University's Chemical Fingerprinting laboratory. Measurements were made by ablating sulphides with a Resonetics (now Australian Scientific Instruments) RESOlution M-50 193 nm, 20 ns pulse duration ArF excimer laser ablation microprobe coupled to a Thermo X-Series II quadrupole ICP-MS. The data reported herein were acquired in several different sessions (of several hours) spanning approximately two years. For all sessions, ablation took place in ultra-pure helium flowing at a rate of 650 ml/min in a Laurin Technic two-volume sample cell that has exceptionally fast wash-out (i.e., < 1.5 s for 99% signal washout), thus affording good spatial resolution (Müller et al. 2009). The vaporized material and helium were combined with argon (750-800 ml/min) and a small amount of nitrogen (6 ml/min), for enhanced

sensitivity (e.g., Hu et al., 2012), outside of the sample cell and approximately 2.5 meters before entering the torch. Ablation and plasma conditions varied from session to session and sample to sample, and are summarized in Table 1.

Quantification of the raw data was conducted with the trace element data reduction scheme in Iolite 3 (Paton et al. 2011) using NIST610 (Jochum et al., 2011) and Fe (i.e., ^{56}Fe or ^{57}Fe since it varied from experiment to experiment) as the external and internal references, respectively. Moreover, periodic measurements of BHVO2g and Po725 were used as reference materials. Note that Fe is a major element in the sulphide grains and as such, its concentration is significantly stoichiometrically controlled. Thus, all trace element concentrations which hinge on EDS/EMP analyses of Fe in individual sulphide grains are representative of the analyzed grains. In order to avoid significantly overestimating concentrations in fractures and inclusions, the internal standard was not forced on a point by point basis, but was instead applied to a representative section of the target mineral. In this way, the data are considered quantitative in the target mineral (e.g. arsenopyrite, pyrite, pyrrhotite) and semi-quantitative in other phases (e.g., inclusions and/or surrounding material) and along fractures, etc. Despite differences in ablation between NIST610 (silicate glass) and sulphides contributing to melting and/or fractionation, similar measurements conducted by Wohlgemuth-Ueberwasser et al. (2015) yielded concentrations within 20% of accepted values when calibrating sulphides with NIST610. We note that a glass reference material is not ideal, however, glasses are often used because there are few if any widely available non-glass reference materials that are satisfactorily homogeneous and cover a wide range of trace elements. The USGS synthetic doped basalt glasses (e.g., GSD-1G) are recommended for similar studies in the future due to their higher Fe content that more closely resembles the sulphides. Fig. 2 demonstrates this to some degree, even for individual

time-slices, as the time-resolved Au concentration from Po725 (Sylvester et al., 2005) calibrated in the way described above are generally within 20% of the accepted value. In the present study, we are interested not in absolute concentrations of a given element, but rather the relationships between elements.

Before conducting the LA ICP-MS analyses, photomicrographs, and domain descriptions (e.g., fracture locations, zoning) were collected as they are required to properly interpret the geochemical data. It is important to make such observations prior to ablation, as LA ICP-MS is a micro-destructive technique that may obliterate or obscure important morphological features.

2.2 Generation of elemental maps and time-slice datasets

The present study uses sulphide element maps and TSD to better understand Au mineralizing processes. For maps, a series of parallel and equal length time-resolved traverses were merged into images using Iolite (e.g., Woodhead et al., 2007) and further subjected to bilinear interpolation between adjacent traverses and 3x3 pixel smoothing to improve the data visualization (see, e.g., Rittner and Müller, 2012). The color scaling of geochemical maps can highlight different features and can have a significant influence on their interpretation. For instance, Fig. 1 shows the Co, Sb, and Ag element maps for an arsenopyrite grain from the Dufferin deposit in the Meguma Terrane (Nova Scotia, Canada) produced using: 1) logarithmic scaling, 2) empirical cumulative density function scaling, 3) linear scaling with +/- 3 standard deviation extrema, and 4) linear scaling with minimum/maximum extrema (note that this causes color saturation at the low and high ends of the spectrum). In addition, note that linear scales tend to obscure low abundances. This figure demonstrates that color scaling alone may highlight various aspects of the element distribution in the sulphide lattice and structure and, therefore, all options must be considered.

In terms of the TSD, each traverse (whether individual or as part of a map) consists of a series of individual time-slice measurements made during one cycle of the quadrupole. In this study, rather than integrating data into a single number, we leave it in its time resolved form consisting of measurements every 0.3 to 1.2 seconds (depending primarily on the number of analytes and dwell time per analyte). In doing so, a higher degree of spatial resolution (compared to conventional spot-based geochemical mapping) is maintained, thus permitting the evaluation of domains such as zoning, fractures and inclusions (Fig. 2). Despite being time-consuming (hours of work), this latter method thus provides the means to treat all the traverse data from a single grain as analogous spot data, but is typically much less time intensive than constructing a map from spots (e.g., Gao et al., 2014; Lawley et al. 2015).

Moreover, rather than comparing TSD data to spot analyses, we compare the TSD data to the accepted values for reference materials. Note that a spot analysis does not have the spatial resolution for some of the features we describe if a large spot size is used. If instead, a small spot size is used, there are down-hole effects (i.e., fractionation of elements based on their volatility). There is fundamentally more noise within individual time-slices but the individual slices are typically within 20% of the accepted values and in a study of this type, the interest is in variations on the scale of orders of magnitude given the extensive use of log based plots.

3. Treatment of data and applications

This section documents a step-wise procedure which should be considered as routine for the treatment and interpretation of LA ICP-MS multi-element analyses. The section is sub-divided to deal separately with elemental paragenesis, the nature of the mineralizing fluid(s), processes that may relate to upgrading of the gold tenor of the samples being studied and hence the deposit they come from, and the use of pyrite geochemistry to discriminate diagenetic versus

metamorphic/hydrothermal origins. Later in this section a variety of statistical techniques for identifying element associations are utilized.

3.1 Elemental paragenesis

Quantitative element distribution maps and traverses performed on sulphide grains, combined with detailed petrographic and/or scanning electron microscopy – energy dispersive X-ray spectrometry (SEM–EDS) studies, provide the basis to establish an elemental paragenesis which is specific to the studied sulphide grains. Therefore, this crucial step underlies the identification of element associations as well as their spatial distribution in the sulphide grain (e.g., core versus rim, fractures, and overgrowths).

Regarding element distribution maps, the intensity of colors highlights the concentration and loci of elements, thus, showing their distribution throughout the grain. Fig. 3 illustrates an example of selected LA ICP-MS element distribution maps produced for an arsenopyrite grain from the Beaver Dam gold deposit and the corresponding elemental paragenesis derived from this is shown in Fig. 4. In this sample, Co mimics the growth zoning which suggests this element has a primary origin. Other elements which are co-spatial with Co are similarly interpreted. Thus, in this case, Ni, Mo Se, Sb and to a lesser extent Au show similar patterns and are therefore also inferred to locally mimic the morphology of the growth zoning. In some cases, elements are seen to overprint the zoning and thus possibly reflect a relatively late primary feature (i.e., Mo, Sb, Se). The uniformly distributed, albeit low concentrations of Ag and Zn suggest they are also in the sulphide lattice either as background concentrations or as local micro-inclusions suggesting a primary origin. Bismuth, Pb and Ag are mainly associated with early fractures (F1) whereas Al, Zn and Mn appear to be relatively late and are associated with later crosscutting fractures (F2), as deduced from petrographic study. Finally, Au seems to also

be broadly associated with both the F1 and F2 fractures as micro-inclusions (Fig. 3), and Ni and Se seem to be reworked given their locally variable concentrations along fractures in addition to Mo and Sb which may reflect remobilization along F1. Thus, based on the interpretation of the elemental distribution maps, four element associations are discerned for this sample; 1) Co-Ni; 2) Mo-Se-Sb (Au-Ag-Zn); 3) Bi-Pb-Ag (Au); and 4) Al-Zn-Mn (Au). We are unaware of any other method whereby this information has previously been generated for sulphides from a mineralized setting.

In contrast to elemental maps, elemental traverses only provide concentrations along selected lines (Fig. 5). Therefore, identification of fractures, growth zoning (e.g., SEM imaging), and inclusions prior to doing the analysis is indispensable to extract information from the dataset (Fig. 5A). An example of a LA ICP-MS traverse done on an arsenopyrite grain from the Meliadine gold district is shown in Fig. 5. The following points are highlighted: 1) Bi, Pb and Co show irregular (i.e., bumpy) patterns, which may reflect both oscillatory zoning and a larger scale zoning, the latter reflected by lower elemental abundances at the top of the sample (to fracture 3) versus below fracture 5 at the bottom; 2) Bi, Pb, and Co are depleted between fractures 3 and 4 and subsequent enrichment in fractures 4 to 5. We suggest that these features may reflect the role of fluids in processes of coupled dissolution and precipitation (i.e., CDP), which is generally discussed more in the context of silicates (e.g., Putnis, 2002; Putnis and Putnis, 2007; Rubatto et al., 2008; Fu et al., 2009; Martin et al., 2011) whereby elements are redistributed; and 3) in contrast, Sb and Mo, which also show some variation in the first part of the traverse (i.e., 25 secs), appear to have been depleted between fractures 4 to 6. Based on these observations, two element associations are noted: 1) Bi-Pb-Co; and 2) Sb-Mo. The latter indicates therefore that, with careful observation, LA ICP-MS traverse data can provide

information equivalent to element distribution maps but with a much shorter acquisition timeframe (e.g., Morey et al., 2008; Gourcerol et al. 2016a). Importantly, we also note that spot analyses cannot provide such meaningful and detailed information and may in fact average out some or all of the details noted here.

It is worth noting that, in a gold exploration context, identifying the sulphide species hosting the gold mineralization must be done prior to any LA ICP-MS map analysis either by spot or traverse mode in order to optimize time and get relevant mapping. Subsequently, it is important to acquire at least one LA ICP-MS map on a host sulphide phase prior to any traverse analysis in order to get a 2D interpretation of zoning and fracture element associations. Moreover, several grains should be analyzed in order to get a qualitative average of element associations.

3.2 Discriminant geochemical plots

In the preceding section, TSD-based analysis yielded element associations for mineralizing events. Given the existence of the event-specific element associations, the next logical avenue of enquiry is the use of the TSD technique in constraining the nature of the mineralizing fluids. In the following section, several plots specifically designed as part of this study are used to address and potentially constrain the nature of the mineralizing fluid, the stages (i.e., number of events) involved in the mineralizing processes, and the origin of elements (i.e., orogenic versus diagenetic).

3.2.1 Nature of the mineralizing fluid

Examination of LA ICP-MS element distribution maps from several studies in orogenic (e.g., Large et al., 2007, 2009, 2011; Lawley et al., 2015) and intrusion-related (e.g., Malartic deposit; Gao et al., 2015) gold deposits indicates that Co and Ni are always present in the sulphide lattice

where they substitute for Fe, thus representing a primary origin reflecting mineral growth (i.e., zonation). When the contents of these latter elements are quantified by element distribution maps, they potentially offer a proxy that can be used to constrain the source and/or nature of the fluid; this aspect is further explored below.

Compilation of the trace element data for several rock types (i.e., felsic to ultramafic) from the Superior Province (Canada) (cf. caption to Fig. 6 for references) is used to construct the series of diagrams - Co/Ni versus Ni, Co versus Co/Ni, and Ni versus Co - (Fig. 6). The distribution of data in these plots clearly indicates, as expected, variations in the Co and Ni contents for different rock suites with the felsic versus ultramafic rocks defining the extreme depletion and enrichment data for the intermediate/lamprophyre rocks defining an intermediary field. These plots are used with the TSD data from the element distribution maps and traverses to constrain the nature of the mineralizing fluids and detect fluid:rock interaction along the fluid pathway.

The application and use of the Co and Ni data is illustrated in Fig. 7 using data from several pyrrhotite (n = 10) and arsenopyrite (n = 3) samples from, respectively, the Musselwhite deposit and the Meliadine gold district (Gourcerol et al., 2016a), as well as arsenopyrite from the Beaver Dam deposit (Fig. 3). Importantly, these data cannot be compared directly to each other as they are for different sulphide phases (i.e., pyrrhotite versus arsenopyrite). However, these samples suggest that the fluids responsible for pyrrhotite deposition at Musselwhite were likely derived from or interacted with ultramafic rocks having intrinsically variable contents of Ni and Co, an interpretation considered necessary in order to explain the four distinctly different fields defined in these plots. The latter is of course based on the assumption that factors controlling element partitioning between fluid and sulphide remain constant. A similar result occurs for the

arsenopyrite data from the Meliadine gold district where two distinct fields are defined. More detailed work at this deposit suggests that the two populations may reflect an early event associated with arsenopyrite crystallization and a second, later event related to the overprinting effects of the Trans-Hudson orogeny (Lawley et al., 2015; Gourcerol et al., 2016). In the last example, arsenopyrite data from Beaver Dam defines two distinct fields which suggest that fluids must have interacted with different reservoirs, one that is relatively mafic/ultramafic and a second of an overall intermediate nature. Given that the former is dominant, the data suggests the fluids interacted more with a mafic reservoir. In conclusion, we note that without use of the approach provided here with the TSD, the distinct fields defined for each of these samples and the interpretations based on this would not have been possible.

3.2.2 Upgrading of gold tenor through ore system reactivation

An important aspect of hydrothermal ore deposits is the longevity of some hydrothermal mineralizing systems, such as is suggested for porphyry deposits (e.g., Sillitoe, 2010), and the consequent complexity of mineral geochemistry and mineral paragenesis that may result. The occurrence of substantial upgrading of gold tenor in some gold systems (e.g., Wagner et al., 2007) is considered to be a result of overprinting events (e.g., Tomkins and Mavrogenes, 2001; Morey et al., 2008; Thomas et al., 2011; Cook et al., 2013; Lawley et al., 2015). Given the importance of recognizing this process in gold mineralized settings, we explore here the use of binary Au versus Ag diagrams for an analyzed sulphide color coded by single elements and element associations (Fig. 8) in order to identify spatial distribution and relationship of each other in the Au:Ag sulphide evolution.

The TSD for the arsenopyrite from Beaver Dam (Figs. 3, 4), for which elemental distribution maps suggest upgrading of Au as well as Ag and Zn along F1 and F2 fracture sets (Fig. 3), is

used to define elemental associations. Note that these element associations cannot be defined with spot analyses. These plots show that Au and Ag contents have a consistent relationship with an Au:Ag ratio of 10:1 and that Co, Ni and Mo-Sb-Se show Au and Ag concentration variations, which confirm their primary origin (Fig. 8A, B, C). In contrast, two elemental remobilizations are suggested for Au and Ag contents: 1) the F1 association Bi-Pb-(Cd-In); and 2) the F2 association Al-Ti-Mn-(V-Cu-Sn-Cr-W)) aligned along F1 and F2 structures (Fig. 8F and G, respectively). Thus, F1, which is defined as a Bi-Pb-In-Cd association, also shows Ag enrichment that may be due to its remobilization and/or introduction of an Ag-rich fluid. The distribution of Se (Fig. 8D) suggests it may also be involved with this remobilization event along F1, but to a lesser extent. The F2 element association of Al-Ti-Mn-V-Cu-Sn-Cr-W (Fig. 8G) collectively shows a high aggregate concentration, which is coincident with the main Au versus Ag trend and is therefore suggestive of upgrading of the precious metals. In Fig. 9, it is apparent that this elemental association is part of the arsenopyrite (i.e., stoichiometric values) rather than due to micro-inclusions. This observation is therefore attributed to the coupled dissolution of earlier arsenopyrite along fractures and precipitation (i.e., CDP process) of a second generation of arsenopyrite which incorporates these new elements. This is a micro-scale zone refining process. Also in regards to Fig. 9, the trend of lower Fe values may represent element remobilization along the F2 fractures, as suggested in Fig. 9H.

Regarding gold remobilization, the presence of the Ag-, Au-Ag- and Au-rich outliers, which are clearly identified in the dataset, provide evidence for the presence of micro-inclusions in the host sulphide (Fig. 8H). The origin of these Au-rich and Ag-rich micro-inclusions, as shown in Fig. 8H, may involve zone refining for the Au- and Ag-rich grains, as present on the F1 and F2 fractures, or a continuation of the primary mineralizing system such that the Au:Ag ratio is

retained. Thus, the use of TSD allows distinction of primary versus remobilization/upgrading of mineralization in sulphide grains.

It should also be noted in regard to Figure 8 that the continuation of the Au-Ag contents in these plots may be more apparent than "real". For instance, variable size micro-inclusions of gold having the same Au:Ag ratio as the invisible Au in the sulphide may contribute to this trend. An example of this would be an inclusion having 1/3 the radius of the laser beam (e.g., 5 μm versus 15 μm) would contribute 1/10 of the value of a gold particle the size of the laser beam and for 1/5 would contribute 1/20 of the value. Thus, it is possible that variable sizes of micro-inclusions can account for the distribution of Au and Ag in the binary plot. Important, however, is that the Au-rich, Ag-poor data points require gold particles with a different Au:Ag ratio and hence origin.

3.2.3. Assessment of element enrichment within pyrite from sediment-hosted gold deposits

Large et al. (2009) used LA ICP-MS generated data from pyrite to assess the origin of four sediment-hosted gold deposits (i.e., Sukhoi Log, Bendigo, Spanish Mountain, and North Carlin Trend). Using these data, they used the chemical signature of pyrite to discriminate early diagenetic versus metamorphic/hydrothermal origin within orogenic- and Carlin-type gold deposits. Based on these latter data and the assigned origin of the various pyrite grains analyzed, Gourcerol et al. (2016a) defined discrimination fields in a binary Ag versus Ni plot (Fig. 10) to distinguish the origin of the analyzed pyrites as well as their associated trace elements.

In order to illustrate the application of this approach and the discrimination diagram (Ag versus Ni), we use TSD for one pyrite grain from the Meadowbank deposit, which is more fully discussed in Gourcerol et al. (2016a). As the various elemental plots show (Fig. 11), this pyrite

records a two-stage growth history involving an early diagenetic stage that was modified, probably via coupled dissolution/precipitation processes, during a later metamorphic- (i.e., orogenic-) related event. As seen in Fig. 10, integration of the TSD with the discriminant fields suggest the early diagenetic pyrite is enriched in Co as well as Bi, Pb and to some extent Mo, whereas the later metamorphic (i.e., orogenic) stage is characterized by enrichment in Au, Se and Mo. Consequently, this approach provides an important means to ascertain the geochemical nature of gold event(s) and establish the origin of the associated metals during pyrite growth in sedimentary rocks.

3.3 Geostatistical analysis

A geostatistical-based set of procedures was applied to compilations of individual TSD for the arsenopyrite grain from the Beaver Dam deposit (Fig. 3). In the following sections, the results of this approach are presented to illustrate how this approach can both complement and confirm the conclusions reached using the elemental distribution maps and discriminant diagrams. Thus, this methodology allows identification and evaluation of elemental affinities, as well as classification of the affinity groups and their relationship to gold mineralizing processes, and, in doing so, may provide and/or confirm the number and character of gold mineralizing events and their respective element associations. Note that the statistical software XLSTAT (2014, Addinsoft, Inc., Brooklyn, NY, USA) was used as a seamless add-on to MS Excel®.

3.3.1. Agglomerative hierarchical clustering

In order to discriminate groups that define element associations in a given sulphide grain, an exploratory agglomerative hierarchical clustering (AHC) can be performed. In this approach, usually presented as a dendrogram plot (Fig. 12), data processing leads to a progressive clustering of elements by a single linkage based on their degrees of similarity (i.e.,

344 concentration) calculated after normalizing the data (i.e., using the same scale). The results are
345 presented as a matrix of element(s) versus element Pearson correlation coefficients (McInnes et
346 al., 2008), in this case using the TSD as seen below.

347 Using the results for the single arsenopyrite grain identified above, the resultant dendrogram
348 plot shows three distinct elemental groups: 1) those associated with the F2 fracture set (see
349 paragenetic sequence in Fig. 4) including Zn-Ag-Au-Cu-Sn-Cr-Al-Mn-W-Ti-V; 2) a primary
350 association or group which includes Co-As-Fe-Ni; and 3) those associated with the F1 fracture
351 set including Mo-Sb-Se-Bi-Pb-Cd-In.

352 It is noted, however, that this approach gives an overview of element associations and must
353 be used with caution as, at a more refined scale, it is limited in that only the closest relationship
354 between elements is illustrated. The consequence of this latter limitation is that minor
355 associations may not be represented, depending on the dataset. Thus, only the highest similarities
356 (i.e., highest correlation values) can be considered as "true" similarities, which for the present
357 case (Fig. 12) would include Ag-Au-(Zn), Mo-Sb, Cd-In, Al-Mn and Ti-V associations. In this
358 regard, it is possible that the later remobilization weakens some of the associations, such as Mo-
359 Sb-Se (Fig. 4), due to Se being remobilized along F1 to join the Bi-Pb-Cd-In grouping.
360 Similarly, the Au-Ag-Zn element association reflects remobilization along the late F2 set from
361 the primary crystallization.

362 **3.3.2. Exploratory statistical methods**

363 Exploratory statistical methods are another approach commonly used in geostatistical
364 studies to analyze data sets and define variables into statistical factors with visual methods.
365 Multidimensional scaling (MDS), principal component analysis (PCA), and linear discriminant

366 analysis (LDA) can be applied to the datasets in order to extract a potential series of factorial
367 variables governing distribution of elements within the sulphides as part of the lattice, as micro-
368 inclusions, or focused along fractures. These methods are performed after a normalization of the
369 data (i.e., using the same scale) based on a matrix of elements versus element Pearson correlation
370 coefficient (McInnes et al., 2008) for the TSD. These methods allow improvement over the main
371 limitation of the AHC as several dimensions are graphically represented. In the following
372 discussion, the TSD generated from the elemental mapping of the same arsenopyrite grain (i.e.,
373 from Beaver Dam deposit; Figs. 3, 4) is used to illustrate these various statistical means of data
374 treatment.

375 ***3.3.2.1. Multidimensional scaling***

376 The MDS method (Wilkinson et al., 1992; Borg and Groenen, 1997, pp. 1-14), similar to
377 the AHC, uses a distance measurement determined from a matrix of Pearson correlation
378 coefficient. Distances are calculated for all the element pairs using standardized data (z-score
379 transformed dataset) to provide a graphical representation of the proximity of elements to each
380 other, using a linear Kruskal loss function reflecting the spatial configuration. Thus, the main
381 factor of discrimination is termed Dimension 1 and the second, Dimension 2. Moreover,
382 elements plotting close together will show a positive correlation which reflects their similar
383 behavior, whereas those elements on opposite sides will show a negative correlation due to
384 dissimilar behavior (e.g., Greenough et al., 2007).

385 The dataset for the selected arsenopyrite defines four distinct groups using MDS (Fig.
386 13A) which are again interpreted in the context of the elemental mapping and paragenesis (Figs.
387 3, 4) : 1) a primary association defined by Co-Fe-Ni-As; 2) a second primary association of Mo-
388 Sb-Se; 3) a secondary association related to the F1 fracture event enriched in Pb-In-Cd-Bi; and

4) another secondary association related to F2 fractures and composed of W-Ti-V-Al-Mn-Sn-Cu-Zn-Ag-Au. Further interpretation of the MDS suggests Dimension 1 may reflect compositions related to fractures whereas Dimension 2 may reflect remobilization/precipitation into micro-inclusions (Fig. 13A). In addition, as pointed out by Greenough et al. (2007), elements tend to organise following Goldschmidt's geochemical classification (Fig. 13B), thus the MDS method can be used to qualitatively identify various fluids equilibrated with the sulphide grain (Greenough et al., 2007). Using this approach, the data suggest a chalcophile affinity for the fluid giving rise to the elements associated with the F1 fracture set versus a lithophile affinity for elements associated with the F2 fracture set. Moreover, the paragenesis of Au can be assessed with MDS combined with LA ICP-MS maps as Au shows a pattern similar to Mo (Fig. 3) along with a similar Goldschmidt classification (Fig. 13B); hence, this infers that these elements share a common temporal relationship and were introduced into this arsenopyrite grain at the same time. The MDS also shows that Au was subsequently remobilized by F1 and F2 events which led to its precipitation and upgrading as invisible to visible micro-inclusions along F1 and F2 (Figs. 3L, 13B).

3.3.2.2. Principal Component Analysis

Like the MDS, the PCA method is a dimension-reduction method applied on a correlation matrix (Pearson coefficient; Grunsky and Smee, 1999) resulting in two-dimensional plots, also referred to as a *correlation circle*. In this plot, elements are distributed as a function of their affinities and dissimilarities (i.e., positive and negative correlations) with respect to two main "factors" which best explain the variability (i.e., PC1 and PC2). These factors represent the main variables within the dataset. In the case of variables positioned close to the center of the circle, it is necessary to check whether the proximities correspond to a "true similarity" with the

412 hypersphere by looking at the correlation circles generated by other factor pairs (i.e., PC1 and
413 PC3). Note that like for the MDS, the PCA method minimizes dimensions but preserves
414 covariance of data, whereas MDS preserves distance between data points (Ghodsi, 2006).

415 The TSD for the same arsenopyrite again shows three to four principal components that
416 together account for the variability of the entire dataset; these are named Primary, F1, F2 and F2'
417 (Fig. 14). Based on the defined grouping, we interpret the associations as follows. The PC1 on
418 the positive side of this axis has two groupings, mainly Bi, In, Pb, Cd and Se and to a lesser
419 extent Fe, Sb and Mo. These associations are attributed to element associations which
420 characterize the F1 fracture event with slight to strong remobilization along it (Fig. 14A). The
421 best example of this F1 association is Se, and to some extent Ni, which is considered as a
422 primary trace element in the arsenopyrite structure (Figs. 3, 4) that was later remobilized along
423 the F1 vector in the correlation circle. Hence, the PC1 negative axis shows F2 element
424 association affinity (e.g., Al, Mn, and V) as they are relatively late in the history of the grain. The
425 positive PC2 axis is composed of the F1 and F2 element associations as well as Ag, Au, Zn and
426 minor Ni, whereas the negative axis is composed of the primary element associations (Fig. 4)
427 which suggests PC2 represents the influence of F2 (Fig. 14A). Finally, the positive PC3 axis is
428 composed mainly of Ag, Au and Zn (F2') and suggests that invisible- to visible micro-inclusions
429 occur along the fracture sets (Fig. 14B). Importantly, the position of Ag, Au and Zn along PC1
430 and PC3 suggests they were subsequently remobilized from F1 and F2 as previously suggested
431 (Figs. 3, 4).

432 ***3.3.2.3. Linear Discriminant Analysis***

433 Finally, the LDA method (Fisher, 1936) uses an approach similar to the PCA technique but
434 varies in the sense that it classifies a dataset into predefined groups such as ranges of

concentration (e.g., Venables and Ripley, 2002, Grunsky et al., 2013) prior to any treatment. Thus, elements are plotted in two dimensional diagrams based on their discrimination scores (i.e., F1 and F2; F1 and F3) as a function of their behavior with an explanatory variable such as Au concentration. Therefore, categorization of Au values as a function of selected elements can provide insight into which elements are closely associated or unrelated to Au mineralization. This approach can also be applied to the element associations related to subsequent Au remobilization (e.g., Wagner et al., 2007).

Thus, application of the LDA approach to the TSD for the same arsenopyrite grain (Fig. 15) shows that Au is strongly associated with Ag and Zn (Fig. 15A, B; note that the latter plot superposes Au values on this vector). In addition, it is also seen that Au is highly associated with Al, Mn, Cu, amongst other elements. and weakly associated with Co, Mo and Sb (Fig. 15C, D). Examining the element associations (Fig. 16), it is clear that elevated Au values (i.e., > 100 ppm) are most strongly associated with the F2 and F1 features whereas Primary' and Primary element associations, that is Mo-Sb-Se and Co-Ni-Fe-As respectively, show a much weaker Au tenor (Fig. 16; from b.d.l. to <100 ppm).

In summary, the LDA plots clearly demonstrate that the gold mineralization was likely initially concentrated as invisible Au in the arsenopyrite (i.e., within its lattice) and subsequently remobilized during F1 and F2 events along with Ag and Zn resulting in Au upgrading as micro-inclusions along the fracture sets.

4. Limitations of LA ICP-MS element distribution analyses and TSD compilation

The data analysis approach described herein, although demonstrably powerful, is not without limitations. These limitations broadly fall into one of two categories: technological and methodological, and are discussed below with possible solutions.

Technically, as noted earlier by Ulrich et al. (2009), a main limitation of all LA ICP-MS element distribution analyses (e.g., maps or traverses) is the beam size (typically > 5 um), which, depending on the geometry of the sample and its internal chemical and physical structure, inevitably results in mixed signals. Chemical and physical variation can also occur in the third dimension, down into the specimen, as the particular laser configuration and target mineral will yield a certain depth of ablation. The latter arise, for example, from low- and high concentration zones and inclusion(s). This issue cannot be forestalled because the size and shape of such features are variable and not known *a priori*. The only possible solution is to remap fine-scale features using a smaller beam size, but even so, the resolution is limited by the smallest beam sizes achievable and the sensitivity and acquisition speed are reduced accordingly. Additionally, the sequential nature of common quadrupole ICP-MS instruments means that the proposed data analysis procedures compare elements that can be derived from different (albeit very close) physical locations. For example, suppose Co and Au are being compared and they are analyzed 250 ms apart in the quadrupole cycle; if the laser is firing at 8 Hz (i.e. every 125 ms) the corresponding Co and Au measurements are related to different material. Often this is insignificant because the comparison is being made from locations belonging to the same feature or domain (e.g., growth zones). However, for micro-inclusions, it can be problematic. This issue affects all instruments having a duty cycle comparable to the laser pulsing period, and is best solved with simultaneous or near-simultaneous detection instruments such as the SpectroMS

(Ardelt et al., 2013) or Tofwerks icpTOF (Gundlach-Graham et al., 2015; Burger et al., 2015). Additional technological advancements that will benefit the type of data analysis conducted in this study include: faster/more sensitive quadrupole ICP-MS instruments (e.g., the latest generation of Thermo and Agilent instruments can collect data ~ 100 times faster than the instrument employed in this study), improved cell designs (i.e. faster wash in/out), and rapid aerosol transport (e.g., Teledyne's Aris), which all contribute to improved spatial resolution and analysis time.

Limitations arising from the analytical method employed here (i.e., traverses) include resampling previously ablated material and the accuracy and statistical significance of individual time-slices of data. The issue of resampling previously ablated material (i.e. as ejecta or condensate) is particularly prevalent when dealing with features with strong concentration contrasts. A similar phenomenon is encountered at grain boundaries between minerals with different major element compositions. This issue can be avoided by mapping with a series of adjacent spots (e.g., Woodhead et al., 2007; Lawley et al., 2015) that can be "pre-cleaned" by a pulse or two of the laser, but this method is typically more time consuming and costly than rastering. Individual traverses of a rastered map can also be pre-cleaned, but this only eliminates contamination from adjacent traverses, not material redeposited ahead of the laser on the current path. There are several issues relating to the accuracy of data acquired and processed as described herein. Firstly, in our opinion, the quantification method employed here is an improvement over simply forcing one internal standard everywhere, but still leaves certain parts of the map as semi-quantitative (e.g., fractures/cracks, inclusions, other minerals). This could be improved by analyzing all the major elements expected in the mapped area and normalizing to 100% as an internal reference (Gagnon et al., 2008; Liu et al., 2008) or by using Iolite's

500 "MinMapping" feature (Paul et al., 2014). Both options improve the accuracy in other phases,
501 but do not necessarily improve the accuracy for inclusions and other features that are smaller
502 than the beam, which can be underestimated or overestimated depending on the ablation
503 efficiency and geometry. Moreover, normalizing to 100% requires that all the major elements be
504 known and analyzed prior to analyzing samples, which can be problematic when keeping the
505 suite of analytes as small as possible. Secondly, the use of a silicate glass (NIST610) as a
506 reference material for sulphide analyses can be problematic as melting and fractionation are
507 expected to limit the accuracy. One study found that the use of NIST610 as an external reference
508 for sulphide analyses with a 193 nm wavelength laser resulted in concentrations generally within
509 20% of the accepted value (Wohlgemuth-Ueberwasser and Jochum, 2015), which is commonly
510 satisfactory for the type of study conducted here. Unfortunately, there are no widely available
511 sulphide reference materials that contain an appropriate suite of trace elements that can be used
512 as an alternative at present. New reference materials may one day become available to alleviate
513 this problem, but in the meantime, the use of fs-lasers could minimize the ablation differences
514 between silicate glass and sulphides (Wohlgemuth-Ueberwasser et al., 2015).

515 Although there are some limitations to the current approach as discussed above, the examples
516 used throughout this study demonstrate that, despite these limitations, the expected element
517 associations are easily identified, suggesting that the data analysis procedure is effective.
518 Different samples, containing different internal chemical and physical structures may be less or
519 more troublesome, and therefore, selection of appropriate samples is a crucial step in this
520 technique. In the event of the latter, there are several technological advances available now that
521 could improve this procedure in terms of quality and speed, and it is expected that once that

technology is more widely adopted among the geoanalytical community, this type of data analysis will be even more powerful.

5. Conclusions

We have shown in this study that, using LA ICP-MS data generated from both elemental mapping and traverses of sulphide grains, considerable insight can be gained regarding the development of the chemical domains in the host and in particular the nature of gold mineralization. By processing these data in the multiple ways presented here, it is possible to enhance our understanding of the nature and origin of gold mineralizing events and, to this end, we have introduced several new concepts to be considered in such studies. The first step, where possible, is to use elemental maps to establish both elemental paragenesis and to identify elemental associations. Given that the map acquisition is both time and cost intensive and that all grains are suitable for such study, we have also explored and shown that traverse data can also provide insight into the nature of gold mineralization. In order to further understand the chemistry of the analyzed material, we also propose innovative procedures for the treatment of time-resolved LA ICP-MS data (i.e., time-slice datasets (TSD)). The use of the TSD in a variety of new discriminant plots (i.e., Co versus Co/Ni; Au versus Ag; Ag versus Ni) and treatment in three-dimensional element plots versus normal binary plots provides possible insight into the origin of the mineralizing fluids and timing of gold mineralization (i.e., diagenetic versus metamorphic/orogenic).

Lastly, conventional geostatistical tools (e.g., MDS, PCA, and DA), which are routinely applied to other geochemical datasets, have been introduced and their application to TSD illustrated. The latter provides further insight into the nature of gold events and also validation of

the conclusions inferred from the other methods used. Thus, we suggest that the integration of the proposed protocol of treating LA ICP-MS data on carefully selected sulphide grains with other geochemical tools commonly applied to gold deposit studies and gold exploration (e.g., fluid inclusions, isotopes) provides the means to better understand the nature and origin of mineralized settings and better discriminate gold mineralizing events and systems.

6. Acknowledgments

The authors gratefully acknowledge Dr. Anne Estrade from the Descartes University (France) for discussions regarding the geostatistical study. Some of the data presented here were acquired as part of our other research and thus benefited from funding from the Geological Survey of Canada Targeted Geoscience Initiative (TGI-4) program, and NSERC CRD and DG type funding to both Drs. D.J., Kontak and P.C. Thurston. We thank Drs. Gagnon, Greenough and an anonymous reviewer for their constrictive comments that helped to substantially improve the manuscript.

7. References

Ardelt, D., Polatajko, A., Primm, O. and Reijnen, M., 2013. Isotope ratio measurements with a fully simultaneous Mattauch–Herzog ICP-MS; Analytical and Bioanalytical Chemistry, v. 405, p. 2987–2994.

Arndt, N.T. and Nesbitt, R.W., 1982. Geochemistry of Munro Township Basalts; *In*: Komatities, (Eds.) Arndt, N.T., E.G. Nisbet, E.G.: London, Allen, and Unwin, p. 309-329.

Arndt, N. T., 1986. Differentiation of Komatiite Flows; Journal of Petrology, v. 27, p. 279-301.

564 Barrie, C.T., Gorton, M.P., Naldrett, A.J. and Hart, T.R., 1991a. Geochemical Constraints On
565 The petrogenesis of The Kamiskotia Gabbroic Complex And Related Basalts, Western Abitibi
566 Subprovince, Ontario, Canada; Precambrian Research, v. 50, p. 173-199.

567 Barrie, C.T. and Shirey, S.B., 1991b. Nd- And Sr-Isotope Systematics for the Kamiskotia-
568 Montcalm Area: Implications for the Formation Of Late Archean Crust in the Western Abitibi
569 Subprovince, Canada; Canadian Journal of Earth Sciences, v. 28, p. 58-76.

570 Barrie, C.T., Corfu, F., Davis, P., Coutts, A.C. and Maceachern, D., 1999. Geochemistry of the
571 Dundonald Komatiite-Basalt Suite and Genesis of Dundeal Ni Deposit, Abitibi Subprovince,
572 Canada; Economic Geology, v. 94, p. 845-866.

573 Beswick, A.E., 1983. Primary Fractionation and Secondary Alteration within an Archean
574 Ultramafic Lava Flow; Contributions to Mineralogy and Petrology, v. 82, p. 221-231.

575 Borg, I. and Groenen, P., 2005. Modern multidimensional scaling: Theory and applications (2nd
576 ed.); Springer series in statistics New York: Springer; doi:10.1007/0-387-28981-X.

577 Bull, S.W., and Large, R.R., 2015, Setting the Stage for the Genesis of the Giant Bendigo Ore
578 System; In: Ore Deposits in an Evolving Earth (Eds.) Jenkin, G.R.T., Lusty, P.A. J., McDonald,
579 I., Smith, M.P., Boyce, A.J. and Wilkinson, J.J.: Geological Society, London, Special
580 Publications, v. 393, p. 1-31.

581 Burger, M., Gundlach-Graham, A., Allner, S., Schwarz, G., Wang, H.A.O., Gyr, L., Burgener,
582 S., Hattendorf, B., Grolimund, D. and Gunther, D., 2015. High-Speed, High-Resolution,
583 Multielemental LA-ICP-TOFMS Imaging: Part II. Critical Evaluation of Quantitative Three-

584 Dimensional Imaging of Major, Minor, and Trace Elements in Geological Samples; Analytical
585 Chemistry, v. 87, p. 8259–8267.

586 Canil, D., 1987. The Geochemistry of Komatiites and Basalts from the Deadman Hill Area,
587 Munro Township, Ontario, Canada; Canadian Journal of Earth Sciences, v. 24, p. 998-1008

588 Cook, N.J., Ciobanu, C.L., Meria, D., Silcock, D. and Wade, B., 2013. Arsenopyrite-Pyrite
589 Association in an Orogenic Gold Ore: Tracing Mineralization History from Textures and Trace
590 Elements; Economic Geology, v. 108, p. 1273-1283.

591 Dinel, E., Saumur, B.M. and Fowler, A.D., 2008. Spherulitic Aphyric Pillow-Lobe Metatholeiitic
592 Dacite Lava of the Timmins Area, Ontario, Canada: A New Archean Facies Formed From
593 Superheated Melts; Economic Geology, v. 103, p. 1365-1378.

594 Dostal, J., Kontak, D.J., Gerel, O., Shellnut, J.G. and Fayek, M., 2015. Cretaceous ongonites
595 (topaz-bearing microleucogranites) from Ongon Khairkan, Central Mongolia: Products of
596 Extreme Magmatic Fractionation and Pervasive Metasomatic Fluid:Rock Interaction; Lithos, v.
597 236-237, p. 173-189.

598 Dostal, J. and Mueller, W.U., 2013. Deciphering an Archean Mantle Plume: Abitibi Greestone
599 Belt, Canada; Gondwana Research, v. 23, p. 493-505.

600 Fan, J. and Kerrich, R., 1997. Geochemical Characteristics of Aluminum Depleted and
601 Undepleted Komatiites and Hree-Enriched Low-Ti Tholeiites, Western Abitibi Greenstone Belt:
602 A Heterogenous Mantle Plume-Convergent Margin Environment; Geochimica et Cosmochimica
603 Acta, v. 61, p. 4723-4744.

604 Feng, R. and Kerrich, R., 1992. Geochemical Evolution of Granitoids from the Archean Abitibi
605 Southern Volcanic Zone and the Pontiac Subprovince, Superior Province, Canada: Implications
606 for Tectonic History and Source Regions; Chemical Geology, v. 98, p. 23-70.

607 Finamore (Hocker), S.M., Gibson, H.L. and Thurston, P.C., 2008. Archean Synvolcanic
608 Intrusions and Volcanogenic Massive Sulphide at the Genex Mine, Kamiskotia Area, Timmins,
609 Ontario; Economic Geology, v. 103, p. 1203-1218.

610 Fisher, R.A., 1936. The Use of Multiple Measurements in Taxonomic Problems; Annals of
611 Eugenics, v. 7 (2), p. 179–188.

612 Fralick, P., Hollings, P., Metsaranta, R. and Heaman, L.M., 2009. Using Sediment Geochemistry
613 and Detrital Zircon Geochronology To Categorize Eroded Igneous Units: An Example From The
614 Mesoarchean Birch-Uchi Greenstone Belt, Superior Province; Precambrian Research, v. 168, p.
615 106-122.

616 Fu, Q., Lu, P., Konishi, H., Dilmore, R., Xu, H., Seyfried Jr., W.E. and Zhu, C., 2009. Coupled
617 Alkali-Feldspar Dissolution and Secondary Mineral Precipitation in Batch Systems: 1. New
618 Experiments at 200°C and 300 bars; Chemical Geology, v. 258; p. 125-135.

619 Gaboury, D. and Pearson, V., 2008. Rhyolite Geochemical Signatures and Association with
620 Volcanogenic Massive Sulphide Deposits: Examples from Abitibi Belt, Canada; Economic
621 Geology, v. 103, p. 1531-1562.

622 Gao, J.-F., Jackson, S.E., Dubé, B., Kontak, D.J. and De Souza, S., 2015. Genesis of the
623 Canadian Malartic, Côté Gold, and Musselwhite gold deposits: Insights from LA-ICP-MS
624 element mapping of pyrite; *In*: Targeted Geoscience Initiative 4: Contributions to the

understanding of Precambrian Lode Gold Deposits and Implications for Exploration, (Eds.) B. Dubé and P. Mercier-Langevin; Geological Survey of Canada, Open File 7852, p. 157-175.

Gagnon, J.E., Fryer, B.J., Samson, I.M. and Williams-Jones, A.E., 2008. Quantitative analysis of silicate certified reference materials by LA-ICPMS without an internal standard: Hournal Analytical At Spectrom; v. 23, p. 1529-1537.

Genna, D. and Gaboury, D., 2015. Deciphering the hydrothermal evolution of a VMS sytem by LA-ICP-MS Using trace elements in pyrite: an example from the Bracemac-McLeod deposits, Abitibi, Canada, and implications for exploration; Economic Geology, v. 110, p. 2087-2108.

Ghodsi, A., 2006. Dimensionality Reduction: A Short Tutorial; Technical report, Department of Statistics and Actuarial Science, University of Waterloo.

Goldstein, S.B. and Francis, D.M., 2008. The Petrogenesis and Mantle Source of Archaean Ferropicrites from the Western Superior Province, Ontario, Canada; Journal of Petrology, v. 49, p. 1729-1753.

Gourcerol, B., Kontak, D.J., Thurston, P.C. and Petrus, J.A., 2016a. Gold and trace element distribution in sulphides from mineralized gold Algoma-type BIFs; Implications for nature of mineralizing fluids, metal sources and deposit models; Accepted by Mineralium Deposita.

Gourcerol, B., Thurston, P.C., Kontak, D.J., Côté-Mantha, O. and Biczok, J., 2016b. Depositional setting of Algoma-type banded iron formation; Precambrian Research, v. 281, p. 47-79.

644 Greenough, J.D., Dostal, J. and Greenough, L.M., 2007. Incompatible Element Ratios in French
645 Polynesia Basalts: Describing Mantle Component Fingerprints; Australian Journal of Earth
646 Sciences, v. 54, p. 947-958.

647 Grunsky, E.C. and Smee, B.W., 1999. The Differentiation Of Soil Types and Mineralization
648 From Multi-Element Geochemistry Using Multivariate Methods and Digital Topography;
649 Geochemical Exploration 1999; Selected Papers From The 19th International Geochemical
650 Exploration Symposium; Journal Of Geochemical Exploration, V. 67 (1-3), P. 287–299.

651 Grunsky, E.C., Drew, L.J., Woodruff, L.G., Friske, P.W.B., And Sutphin, D.M., 2013. Statistical
652 Variability Of The Geochemistry And Mineralogy Of Soils In The Maritime Provinces Of
653 Canada And Part Of The Northeast United States; Geochemistry: Exploration,
654 Environment, Analysis, V. 13, P. 249-266.

655 Gundlach-Graham, A.W., Burger, M., Allner, S., Schwarz, G., Wang, H.A.O., Gyr, L.,
656 Grolimund, D., Hattendorf, B. and Gunther, D., 2015. High-speed, high-resolution, multi-
657 elemental LA–ICP–TOFMS imaging: Part I. instrumentation and two-dimensional imaging of
658 geological samples; Analytical Chemistry, v. 87, p. 8250-8258.

659 Hineman, A. and Stephan, C., 2014. Effect of Dwell Time on Single Particle Inductively Couled
660 Plasma Mass Spectrometry Data Acquisition Quality; Journal of Analytical Atomic
661 Spectrometry, v. 29, p. 1252-1257.

662 Hollings, P. and Wyman, D.A., 1999. Trace Element And Sm-Nd Systematics of Volcanic and
663 Intrusive Rocks from the 3 Ga Lumby Lake Greenstone Belt, Superior Province; Evidence For
664 Archean Plume-Arc Interaction; Lithos, v. 46, p. 189-213.

Hollings, P. and Kerrich, R., 1999a. Trace Element Systematics of Ultramafic and Mafic Volcanic and Intrusive Rocks from the 3 Ga North Caribou Greenstone Belt, Northwestern Superior Province; Precambrian Research, v. 93, p. 257-279.

Hollings, P. and Kerrich, R., 1999b. Komatiite-Basalt-Rhyolite Volcanic Associations In Northern Superior Province Greenstone Belts; Significance Of Plume-Arc Interaction In The Generation Of The Proto Continental Superior Province; Lithos, v. 46, p. 137-161.

Hollings, P., Stott G.M. and Wyman D.A., 2000. Trace Element Geochemistry of the Meen-Dempster Greenstone Belt, Uchi Subprovince, Superior Province, Canada: Back-Arc Development on the Margins of an Archean Protocontinent; Canadian Journal of Earth Sciences, v. 37, p. 1021-1038.

Hu, Z., Liu, Y., Gao, S., Liu, W., Zhang, W., Tong, X., Lin, L., Zong, K., Li, M., Chen, H., Zhou, L. and Yang, L., 2012. Improved in situ Hf isotope ratio analysis of zircon using newly designed X skimmer cone and jet sample cone in combination with the addition of nitrogen by laser ablation multiple collector ICP-MS; Journal of Analytical Atomic Spectrometry, v. 27(9), p. 1391-1399.

Hollings, P. and Kerrich, R., 2000. An Archean Arc Basalt-Nb-Enriched Basalt-Adakite Association: The 2.7 Ga Confederation Assemblage of the Birch-Uchi Greenstone Belt, Superior Province; Contributions to Mineralogy and Petrology, v. 139, p. 208-226.

Innes, D.G., 1978. Some Chemical Characteristics of Ultramafic and Tholeiitic Rocks, Newton Township, District Of Sudbury; Ontario Geological Survey, Miscellaneous Paper 82, p. 225-227.

685 Janvier, V., Castonguay, S., Mercier-Langevin, P., Dubé, B., McNicoll, V., Pehrsson, S., Malo,
686 M., De Chavigny, B. and Cote-Mantha, O., 2015. Preliminary results of geology of the Portage
687 deposit, Meadowbank gold mine, Churchill Province, Nunavut, Canada; Geological Survey of
688 Canada, Current Research 2015-2, 18 p.

689 Jenner, F.E. and Arevalo, R.D. Jr., 2016. Major and trace element analysis of natural and
690 experimental igneous systems using LA-ICP-MS; Elements, v. 12, p. 311-316.

691 Jochum, K.P., Weis, U., Stoll, B., Kuzmin, D., Yang, Q., Raczek, I., Jacob, D.E., Stracke, A.,
692 Gunther, D. and Enzweiler, J., 2011. Determination of Reference Values for NIST SRM 610-617
693 Glasses Following ISO Guidelines; Geostandards and Geoanalytical Research, v. 35(4), p. 397–
694 429.

695 Kerrich, R., Polat, A., Wyman, D.A. and Hollings, P., 1999. Trace Element Systematics of Mg-,
696 To Fe-Tholeiitic Basalt Suites of the Superior Province: Implications for Archean Mantle
697 Reservoirs and Greenstone Belt Genesis; Lithos, v. 46, p. 163-187.

698 Kerrich, R., Polat, A. and Xie, Q., 2008. Geochemical Systematics of 2.7 Ga Kinojevis Group
699 (Abitibi), and Manitouwadge and Winston Lake (Wawa) Fe-Rich Basalt-Rhyolite Associations:
700 Backarc Rift Oceanic Crust? ; Lithos, v. 101, p. 1-23.

701 Kitayama, Y.C. and Francis, D.M., 2014. Iron-Rich Alkaline Magmatism in the Archean Wawa
702 Greenstone Belts (Ontario, Canada); Precambrian Research 252, p. 53-70.

703 Kontak, D.J., 2015. Applications and Implications of Trace Element Chemistry and Elemental
704 Mapping of Ore Minerals to Hydrothermal Ore Deposit Discrimination and Genetic Models;

Geological Association of Canada–Mineralogical Association of Canada Joint Annual Meeting, May 3-7, Montreal, Quebec, Program with abstracts, vol. 38, p. 293.

Kontak, D.J., Horne, R.J., Creaser, R.A., Petrus, J. and Archibald, D., 2013. A Petrological and Geochronological Study of a 360 Ma Metallogenic event in Maritime Canada with Implications for Lithophile-Metal Mineralization in the Canadian Appalachians; Canadian Journal of Earth Sciences, vol. 50, 1147-1163.

Kontak, D.J., Smith, P. K. and Reynold, P.H., 1993.Geology and Ar/Ar Geochronology of the Beaver Dam Gold Deposit, Meguma Terrane, Nova Scotia, Canada: Evidence for Mineralization at 370 Ma; Economic Geology, v. 88, p. 139-170.

La Fleche, M.R., Dupuy, C. and Bougault, H., 1992. Geochemistry and Petrogenesis of Archean Mafic Volcanic Rocks of the Southern Abitibi Belt, Quebec; Precambrian Research, v. 57, p. 207-241.

La Fleche, M.R. and Dupuy, C., 1992. Tholeiitic Volcanic Rocks of the Late Archean Blake River Group, Southern Abitibi Greenstone Belt: Origin and Geodynamic Implications; Canadian Journal of Earth Sciences, v. 29, p. 1448-1458.

Lafrance, B., Mueller, W.U., Daigneault, R. and Dupras, N., 2000. Evolution Of A Submerged Composite Arc Volcano: Volcanology And Geochemistry of the Normetal Volcanic Complex, Abitibi Greenstone Belt, Quebec, Canada; Precambrian Research 101, p. 277-311.

Lahaye, Y., Arndt N.T., Byerly, G. R., Chauvel, C., Fourcade, S. and Gruau, G., 1995. The Influence of Alteration on the Trace-Element and Nd Isotopic Compositions of Komatiites; Chemical Geology, v. 126, p. 43-64.

Lahaye, Y. and Arndt N.T., 1996. Alteration of a Komatiite Flow from Alexo, Ontario, Canada; Journal of Petrology, v. 37, p. 1261-1284.

Large, R.R., Bull, S.W. and Maslennikov, V.V., 2011. A Carbonaceous Sedimentary Source-Rock Model for Carlin- Type and Orogenic Gold Deposits; Economic Geology, v. 106, p. 331-358.

Large, R.R., Danyushevsky, L., Hollit, C., Maslennikov, V., Meffre, S., Gilbert, S., Bull, S., Scott, R., Emsbo, P., Thomas, H., Singh, B. and Foster, J., 2009. Gold and Trace Element Zonation in Pyrite Using a Laser Imaging Technique: Implications for the Timing of Gold in Orogenic and Carlin-Style Sediment-Hosted Deposits; Economic Geology, v. 104, p. 635-668.

Large, R.R., Maslennikov, V.V., Robert, F., Danyushevsky, L.V. and Chang, Z., 2007. Multistage Sedimentary and Metamorphic Origin of Pyrite and Gold in the Giant Sukhoi Log Deposit, Lena Gold Province, Russia; Economic Geology, v. 102, p. 1233-1267.

Lawley, C.J.M., Creaser, R.A., Jackson, S., Yang, Z., Davis, B., Pehrsson, S., Dubé, B., Mercier-Langevin, P., and Vaillancourt, D., 2015c. Unravelling the Western Churchill Province Paleoproterozoic Gold Metallotect: Constraints from Re-Os Srsenopyrite and U-Pb Xenotime Geochronology and LA-ICP-MS Arsenopyrite Trace Element Chemistry at the BIF-hosted Meliadine Gold District, Nunavut, Canada; Economic Geology, v. 110, p. 1425-1454.

Liu, Y., Hu, Z., Gao, S., Günther, D., Xu, J., Gao, C. and Chen, H., 2008. In situ analysis of major and trace elements of anhydrous minerals by LA-ICP-MS without applying an internal standard; Chemical Geology, v. 257, p. 34–43.

Longerich, H. P., Jackson, S. E. and Günther, D., 1996. Inter-laboratory note. Laser ablation inductively coupled plasma mass spectrometric transient signal data acquisition and analyte concentration calculation; Journal of Analytical Atomic Spectrometry, v. 11(9), p. 899-904.

McDivitt, J.A., 2016. Gold Mineralization in the Missanabie-Renabie District of the Wawa Subprovince (Missanabie, Ontario, Canada); Master Thesis in Geology, Laurentian University, 179 p.

Marchese, S., Gentili, A., Perret, D., Ascenzo, G.D. and Pastori, F., 2003. Quadrupole Time-of-Flight versus Triple-Quadrupole Mass Spectrometry for the Determination of Nonsteroidal Anti-inflammatory Drugs in Surface Water by Liquid Chromatography/Tandem Mass Spectrometry; Rapid Communications Mass Spectrometry, v. 9, p. 879-886.

Maurice, C., Francis, D.M. and Madore, L., 2003. Constraints on Early Archean Crustal Extraction and Tholeiitic-Komatiitic Volcanism in Greenstone Belts of Northern Superior Province; Canadian Journal of Earth Sciences, v. 40, p. 431-445.

Martin, L.A.J., Ballevre, M., Boulvais, P., Halfpenny, A., Vanderhaeghe, O., Duchene, S. and Deloule, E., 2011. Garnet Re-Equilibration by Coupled Dissolution-Reprecipitation: Evidence from Textural, Major Element and Oxygen Isotope Zoning of “Cloudy” Garnet; Journal of Metamophic Geology, v. 29, p. 213-231.

Maurice, C., David, J., Bedard, J.H. and Francis D.M., 2009. Evidence for a Widespread Mafic Cover Sequence and its Implications for Continental Growth in the Northeastern Superior Province; Precambrian Research, v. 168, p. 45-65.

766 McInnes, M., Greenough, J.D., Fryer, B. and Wells, R., 2008. Trace elements in Native Gold by
767 Solution ICP-MS and their use in Mineral Exploration: A British Columbia example; Applied
768 Geochemistry, v. 23, p. 1076-1085.

769 Mercier-Langevin, P., Dubé, B., Hannington, M.D., Richer-Lafleche, M. and Gosselin, G., 2007.
770 The La Ronde Penna Au-Rich Volcanogenic Massive Sulphide Deposit, Abitibi Greenstone Belt,
771 Québec: Part II. Lithogeochemistry and Paleotectonic Setting; Economic Geology, v. 102, p.
772 611-631.

773 Morey, A.A., Tomkins, A.G., Bierlein, F.P., Weinberg, R.F. and Davidson, G.J., 2008. Bimodal
774 Distribution of Gold in Pyrite and Arsenopyrite: Examples from the Archean Boorara and
775 Bardoc Shear Systems, Yilgarn Craton, Western Australia; Economic Geology, v. 103, p. 599–
776 614.

777 Müller, W., Shelley, M., Miller, P. and Broude, S., 2009. Initial performance metrics of a new
778 custom-designed ArF excimer LA-ICPMS system coupled to a two-volume laser-ablation cell;
779 Journal of Analytical Atomic Spectrometry, v. 24(2), p. 209-214.

780 Nesbitt, H.W., Young, G.M. and Bosman, S.A., 2009. Major and Trace Element Geochemistry
781 and Genesis of Supracrustal Rocks of the North Spirit Lake Greenstone Belt, Nw Ontario,
782 Canada; Precambrian Research, v. 174, p. 16-34.

783 Neyedley, K., Hanley, J.J., Fayek, M. and Kontak, D.J., 2016. Textural, fluid inclusion, and
784 stable O isotope constraints on vein formation and gold precipitation, 007 deposit, Bissett,
785 Manitoba, Canada; Economic Geology, *In press*.

786 Oswald, W., Castonguay, S., Dubé, B., McNicoll, V.J., Biczok, J., Malo, M. and Mercier-
787 Langevin, P., 2015. Geological Setting of the World-Class Musselwhite Gold Mine, Superior
788 Province, Northwestern Ontario, and Implications for Exploration; *In*: Targeted Geoscience
789 Initiative 4: Contributions to the Understanding of Precambrian Lode Gold Deposits and
790 Implications for Exploration, (Eds.) B. Dubé and P. Mercier- Langevin; Geological Survey of
791 Canada, Open File 7852, p. 69–84

792 Parks, J., Lin, S., Davis, D.W., Yang, X., Creaser, R.A. and Corkery, M.T., 2014. Meso- And
793 Neoarchean Evolution of the Island Lake Greenstone Belt and the Northwestern Superior
794 Province: Evidence from Lithogeochemistry, Nd Isotope Data, and U-Pb Zircon Geochronology;
795 Precambrian Research, v. 246, p. 160-179

796 Paton, C., Hellstrom, J., Paul, B.,Woodhead, J. and Hergt, J., 2011. Iolite: Freeware for the
797 visualisation and processing of mass spectrometric data; Journal of Analytical Atomic
798 Spectrometry, v. 26, p. 2508-2518.

799 Paul, B., Woodhead, J.D., Paton, C., Hergt, J.M., Hellstrom, J. and Norris, C.A., 2014. Towards
800 a Method for Quantitative LA-ICP-MS Imaging of Multi-Phase Assemblages: Mineral
801 Identification and Analysis Correction Procedures; Geostandards and Geoanalytical Research, v.
802 38, p. 253–263.

803 Picard, C.P. and Piboule, M., 1986. Pétrologie des Roches Volcaniques du Sillon de Roches
804 Vertes Archéennes De Matagami - Chibougamu à l'Ouest De Chapais (Abitibi Est, Québec). 2.
805 Le Groupe Hautement Potassique d'Opemisca; Canadian Journal of Earth Sciences, v. 23, p.
806 1169-1189.

807 Piercey, S.J., Chaloux, E.C., Peloquin, A.S., Hamilton, M. A. and Creaser, R.A., 2008.
808 Synvolcanic and Younger Plutonic Rocks from the Blake River Group: Implications for
809 Regional Metallogenesis; Economic Geology, v. 103, p. 1243-1268.

810 Polat, A., Kerrich, R. and Wyman, D.A., 1999. Geochemical Diversity in Oceanic Komatiites
811 and Basalts from the Late Archean Wawa Greenstone Belts, Superior Province, Canada: Trace
812 Element and Nd Isotope Evidence for a Heterogeneous Mantle; Precambrian Research, v. 94, p.
813 139-173.

814 Polat, A. and Kerrich, R., 2000. Archean Greenstone Belt Magmatism and the Continental
815 Growth-Mantle Evolution Connection: Constraints from Th-U-Nb-Lree Systematics of the 2.7
816 Ga Wawa Subprovince, Superior Province, Canada; Earth and Planetary Science Letters, v. 175,
817 p. 41-54.

818 Polat, A. and Münker, C., 2004. Hf-Nd Isotope Evidence For Contemporaneous Subduction
819 Processes in the Source of Late Archean Arc Lavas from the Superior Province, Canada;
820 Chemical Geology, v. 213, p. 403-429.

821 Polat, A., 2009. The Geochemistry of Neoarchean (Ca. 2700 Ma) Tholeiitic Basalts; Transitional
822 to Alkaline Basalts; and Gabbros; Wawa Subprovince; Canada: Implications for Petrogenetic
823 and Geodynamic Processes; Precambrian Research, v. 168, p. 83-105.

824 Polat, A., Longstaffe, F.J., Weisener, C., Fryer, B.J., Frei, R. and Kerrich, R., 2012. Extreme
825 Element Mobility during Transformation of Neoarchean (Ca. 2.7 Ga) Pillow Basalts to a
826 Paleoproterozoic (Ca. 1.9 Ga) Paleosol, Schreiber Beach, Ontario, Canada; Chemical Geology,
827 v. 326-327, p. 145-173.

828 Putnis, A. and Putnis, C.V., 2010. The mechanism of re-equilibration of solids in the presence of
829 a fluid phase; Journal of Solid State Chemistry, v. 180, p. 1783-1786.

830 Putnis, C.V., Geisler, T. Schmid-Beurmann, P., Stpehan, T. and Giampaolo, C., 2007. An
831 experimental study of the replacement of leucite by analcime; American Mineralogist, v. 92, p.
832 19-26.

833 Putnis, A. 2002. Mineral replacement reactions: from macroscopic observations to microscopic
834 mechanisms; Mineralogical Magazine, v. 66, p. 689-708.

835 Rinne, M. and Hollings, P., 2013. The Characteristics and Origin of the Big Lake Mafic-
836 Ultramafic-Hosted Volcanogenic Massive Sulphide Occurrence, Marathon, Ontario, Canada;
837 Economic Geology, v. 108, p. 719-738.

838 Rittner, M. and Müller, W., 2012. 2D mapping of LA-ICPMS trace element distributions using
839 R. Computers & Geosciences, v. 42, p. 152-161.

840 Rubatto, D., Mutener, O., Barnhoorn, A, and Gregory, C., 2008. Dissolution-Reprecipitation of
841 Zircon at Low-Temperature, High-Pressure Conditions (Lanzo Massif, Italy); American
842 Mienralogist, v. 93, p. 1519-1529.

843 Sangster, A.L. and Smith, P.K., 2007. Metallogenic summary of the Meguma gold deposits,
844 Nova Scotia; In Goodfellow, W.D. (Eds.), Mineral Deposits of Canada: a Synthesis of Major
845 Deposit-types, District Metallogeny, the Evolution of Geological Provinces, and Exploration
846 Methods. Geological Association of Canada, Mineral Deposits Division, Special Publication,
847 vol. 5, pp. 723-732.

848 Sillitoe, R.H., 2010. Porphyry Copper Systems; Economic Geology, v. 105, p. 3-41.

849 Sproule, R.A., Lesher, C.M., Ayer J.A., Thurston P.C. and Herzberg, C.T., 2002. Spatial and
850 Temporal Variations in the Geochemistry of Komatiites and Komatiitic Basalts in the Abitibi
851 Greenstone Belt; Precambrian Research, v. 115, p. 153-186.

852 Stone, W.E., Crocket, J.H., Fleet, M.E., 1993. Sulphide-Poor Platinum-Group Mineralization in
853 Komatiitic Systems; Boston Creek Flow, Layered Basaltic Komatiite, Abitibi Belt, Ontario;
854 Economic Geology, v. 88, p. 817-836.

855 Stone, W.E., Crocket, J.H., Dickin, A.P. and Fleet, M.E., 1995. Origin of Archean Ferropicrites:
856 Geochemical Constraints from the Boston Creek Flow, Abitibi Greenstone Belt, Ontario,
857 Canada; Chemical geology, v. 121, p. 51-71.

858 Stone, W.E., Crocket, J.H., Fleet, M.E. and Larson M.S., 1996. Pge Mineralization in Archean
859 Volcanic Systems: Geochemical Evidence from thick, differentiated Mafic-Ultramafic Flows,
860 Abitibi Greenstone Belt, Ontario, and Implications for Exploration; Journal of Geochemical
861 Exploration, v. 56, p. 237-263.

862 Stone, M.S. and Stone, W.E., 2000. A Crustally Contaminated Komatiitic Dyke-Sill-Lava
863 Complex, Abitibi Greenstone Belt, Ontario; Precambrian Research, v. 102, p. 21-46.

864 Sylvester P.C., Cabri L.J., Turbett M.N., McMahon G., Laflamme J.G.H. and Peregoedova A.,
865 2005. Synthesis and evaluation of a fused pyrrhotite standard reference material for platinum-
866 group element and gold analyses by laser ablation-ICPMS; Geological Survey of Finland, Espoo,
867 Finland, 16-20, 10th International Platinum Symposium; Platinum-group elements; from genesis
868 to beneficiation and environmental impact; extended abstracts.

869 Thomas, H.V., Large, R.R., Bull, S.W., Maslennikov, V., Berry, R.F., Fraser, R., Froud, S. and
870 Moye, R., 2011. Pyrite and Pyrrhotite Textures and Compositions in Sediments, Laminated
871 Quartz Veins, and Reefs at Bendigo Gold Mine, Australia: Insights for Ore Genesis; Economic
872 Geology, v. 106, p. 1–31.

873 Tomkins, A.G. and Mavrogenes, J.A., 2001. Redistribution of Gold within Arsenopyrite and
874 Löllingite during pro- and retrograde Metamorphism: Application to Timing of Mineralization;
875 Economic Geology, v. 96, p. 525−534.

876 Thurston, P.C. and Fryer, B.J., 1983. The Geochemistry of Repetitive Cyclical Volcanism from
877 Basalt through Rhyolite in the Uchi-Confederation Greenstone Belt, Canada; Contributions to
878 Mineralogy and Petrology, v. 83, p. 204-226.

879 Ujike, O. and Goodwin, A.M., 1987. Geochemistry and Origin of Archean Felsic Metavolcanic
880 Rocks, Central Noranda area, Quebec, Canada; Canadian Journal of Earth Sciences, v. 24, p.
881 2551-2567.

882 Ujike, O., Goodwin, A.M. and Shibata, T., 2007. Geochemistry and Origin of Archean Volcanic
883 Rocks from the Upper Keewatin Assemblage (Ca. 2.7 Ga), Lake of the Woods Greenstone Belt,
884 Western Wabigoon Subprovince, Superior Province, Canada; The Island Arc, v. 16, p. 191-208.

885 Ulrich, T., Kamber, B.S., Jugo, P.J. and Tinkham, D.K., 2009. Imaging Element-Distribution
886 Patterns in Minerals by Laser Ablation-Inductively Coupled Plasma-Mass Spectrometry (LA-
887 ICP-MS); Canadian Mineralogist, v. 47, p. 1001-1012.

888 Wagner, T., Klemd, R., Wenzel, T. and Mattson B., 2007. Gold Upgrading in Metamorphosed
889 Massive Sulphide Ore Deposits: Direct Evidence from Laser-Ablation-Inductively Coupled
890 Plasma-Mass Spectrometry Analysis of Invisible Gold; Geology, v. 35, n. 9, p. 775-778.

891 Warren, M.R., Hanley, J.J., Ames, D.E. and Jackson, S.E., 2015. The Ni–Cr–Cu content of
892 biotite as pathfinder elements for magmatic sulfide exploration associated with mafic units of the
893 Sudbury Igneous Complex, Ontario, Canada; Journal of Geochemical Exploration, v. 153, p. 11–
894 29.

895 Wohlgemuth-Ueberwasser CC, Jochum, KP (2015) Capability of fs-LA-ICP-MS for sulphide
896 analysis in comparison to ns-LA-ICP-MS: Reduction of laser induced matrix effects?. J Anal At
897 Spectrom 30:2469-2480

898 Woodhead, J., Hellstrom, J., Hergt, J., Greig, A., and Maas, R., 2007, Isotopic and elemental
899 imaging of geological materials by laser ablation Inductively Coupled Plasma mass
900 spectrometry: Journal of Geostandards and Geoanalytical Research, v. 31, p. 331-343.

901 Wilkinson, L., Hill, M. and Vang, E., 1992. SYSTAT: Statistics. Version 5.2 edition; Systat,
902 Evanston, Illinois, USA.

903 Wyman, D.A. and Kerrich, R., 1993. Archean Shoshonitic Lamprophyres of the Abitibi
904 Subprovince, Canada: Petrogenesis, Age, and Tectonic Setting; Journal of Petrology, v. 34, p.
905 1067-1109.

906 Wyman, D.A. and Hollings, P., 1998. Long-Lived Mantle-Plume Influence on an Archean
907 Protocontinent; Geochemical Evidence from the 3 Ga Lumby Lake Greenstone Belt, Ontario,
908 Canada; Geology, v. 26, p. 719-722.

Wyman, D.A., 1999. A 2.7 Ga Depleted Tholeiite Suite: Evidence of Plume-Arc Interaction in the Abitibi Greenstone Belt, Canada; Precambrian Research, v. 97, p. 27-42.

Wyman, D.A., Ayer, J.A. and Devaney J.R., 2000. Niobium-Enriched Basalts from the Wabigoon Subprovince, Canada: Evidence for Adakitic Metasomatis above an Archean Subduction Zone; Earth and Planetary Science Letters, v. 179, p. 21-30.

Wyman, D.A., Kerrich, R. and Polat, A., 2002. Assembly of Archean Cratonic Mantle Lithosphere and Crust: Plume-Arc Interaction in the Abitibi-Wawa Subduction-Accretion Complex; Precambrian Research, v. 115, p. 37-62.

Wyman, D.A. and Kerrich R., 2009. Plume and Arc Magmatism in the Abitibi Subprovince: Implications for the Origin of Archean Continental Lithospheric Mantle; Precambrian Research, v. 168, p. 4-22

8. Figure Captions

Fig.1. LA ICP-MS element maps for an arsenopyrite grain from the Dufferin deposit, Meguma Terrane (Nova Scotia, Canada). The maps show the distribution of Co (left column), Sb (middle column) and Ag (right column) with four different color scales: 1) logarithmic concentration scale between the minimum and maximum values (A, B, C); 2) empirical cumulative distribution function scale between the minimum and maximum values (D, E, F); 3) linear concentration

scale between the data median +/- 3 standard deviations (G, H, I); and 4) linear concentration scale between minimum/maximum values (J, K, L). Note that straight lines, which are mainly seen in the Sb maps, correspond to earlier LA traverses done on the grain. The X and Y axis scale is given in microns.

Fig. 2. Concentrations (in ppm) for selected elements of varying contents plotted against elapsed time in multiples of single cycles (i.e., 0.3 seconds) of the quadrupole (i.e., 0.3, 1.2, 3 and 5 seconds) for traverses. As discussed in the text, the time for a single cycle depends on the number of analytes and dwell time per analyte. A) to C) Element concentrations of Al, Ni and Co in the BHVO2G standard. D) Element concentration of Au in the Po725 standard (Sylvester et al. 2005). Note the dashed black line and darker grey field represent the expected values (i.e., Al in BHVO2G 72000 ± 1000 ppm; Ni in BHVO2G 116 ±14 ppm; Co in BHVO2G 44 ± 4 ppm; Au in Po725 44.5 ± 2.5 ppm), whereas lighter grey fields refer to ± 20% of accepted values. Thus, this figure illustrates that the shorter time of acquisition is the best option to identify micro-inclusions of, for example, sulphides. Note that the concentration values for individual time slices are usually within 20% of the accepted value.

Fig. 3. LA ICP-MS element maps showing the distribution of selected elements in part of an arsenopyrite grain from the Beaver Dam deposit, Meguma Terrane (Nova Scotia, Canada). A) to J) Elemental maps plotted as concentrations scaled between the data median +/- 3 standard deviations (in ppm). K, L) Element maps plotted as logarithmic concentrations scaled between the minimum and maximum values (in weight %). Note the following features illustrated in the maps: 1) the black dashed lines shown in A represent primary growth zoning; 2) the white lines represent two sets of fractures referred to as F1 (dashed lines) or F2 (dotted lines). Note that the straight lines, which are mainly seen in the Sb maps, correspond to earlier AL traverses done on the grain. Scale is given in microns.

Fig. 4. An elemental paragenesis for the arsenopyrite grain from the Beaver Dam deposit (Nova Scotia, Canada) shown in Fig. 3. Note that the elemental paragenesis was derived based on the distribution of the selected elements in the elemental maps for this grain in addition to the presence of fractures (F1, F2).

Fig. 5. Quantitative LA ICP-MS elemental profiles (in ppm) acquired from a traverse across an arsenopyrite grain from the Meliadine gold district (Nunavut, Canada). A) Reflected light photomicrograph of the analyzed arsenopyrite grain. The solid black line represents the traverse whereas the numbered (1 to 6) dashed black lines represent micro-fractures identified based on reflect light observations. B) concentration profiles for selected elements along the traverse shown in image A. Note that the dashed black lines refer to the micro-fractures identified in image A. Abbreviations: Aspy: Arsenopyrite; Po: Pyrrhotite.

Fig. 6. Binary plots showing the distribution of Co, Ni and Co/Ni for various rock types from the Archean Superior Province (Canada): A) Co/Ni versus Ni; B) Co versus Co/Ni; and C) Ni versus Co. The distribution of the elements and elemental ratios in these plots define the corresponding

982 compositional fields: pink corresponds to felsic, light green to mafic, light blue to ultramafic,
983 light purple to lamprophyre and the dashed field to intermediate rocks. Data used to define the
984 fields are from the following sources: Arndt and Nesbitt, 1982; Arndt, 1986; Barrie et al., 1991a,
985 b, 1999; Beswick, 1983; Canil, 1987; Dinel et al., 2008; Dostal and Muller, 2013; Fan and
986 Kerrich, 1997; Feng and Kerrich, 1992; Finamore et al., 2008; Fralick et al., 2009; Gaboury and
987 Pearson, 2008; Goldstein and Francis, 2008; Hollings and Wyman, 1999; Hollings and Kerrich,
988 1999a, b; Hollings et al., 2000; Hollings and Kerrich, 2000; Innes, 1978; Kerrich et al., 1999,
989 2008; Kitayama and Francis, 2014; La Fleche et al., 1992; La Fleche and Dupuy, 1992; Lafrance
990 et al., 2000; Lahaye et al., 1995; Lahaye and Arndt, 1996; Maurice et al., 2003, 2009; Merci-
991 Langevin et al., 2007; Nesbitt et al., 2009; Parks et al., 2014; Picard and Piboule, 1986; Piercey
992 et al., 2008; Polat et al., 1999, 2012; Polat and Kerrich, 1999; Pollat and Münker, 2004; Pollat,
993 2009; Rinne and Hollings, 2013; Sproule et al., 2002; Stone et al., 1993, 1995, 1996; Stone and
994 Stone, 2000; Thurston and Fryer, 1983; Ujike and Goodwin, 1987; Ujike et al., 2007; Wyman
995 and Kerrich, 1993; Wyman and Kerrich, 1993, 2009; Wyman and Hollings, 1998; Wyman, 1999;
996 Wyman et al., 2000, 2002.

997

998

999 Fig. 7. Distribution of elements (Co, Ni) and elemental ratios (Co/Ni) based on TSD from LA
1000 ICP-MS analyses for both traverse and mapping modes of sulphides from the Musselwhite,
1001 Meliadine and Beaver Dam deposits. The data are shown in the same discriminant diagrams as
1002 seen in the Figure 6. A) Co/Ni versus Ni; B) Co versus Co/Ni; and C) Ni versus Co. The data
1003 plotted are based on 10 pyrrhotite samples from the Musselwhite deposit, 3 arsenopyrite grains

from the Meliadine gold district, and a single element distribution map for arsenopyrite from the Beaver Dam deposit.

Fig. 8. Binary element plots (in ppm) of Au versus Ag based on the TSD for the mapped arsenopyrite grain from the Beaver Dam deposit (Nova Scotia, Canada); there are approximately 39800 data points represented in this diagram. Note that in Figures A to G the data points are colour coded (i.e., cold to hot) in order to reflect enrichment in either an element or elemental association; see text for further discussion. Figure H is a representative summary plot showing an interpretation of the elemental distributions. Note the dashed red line in panels A to G represents the detection limit for Au that the F1 element association consists of Bi-Pb-In-Cd, and the F2 element association consists of Al-Ti-Mn-V-Cu-Sn-Cr-W.

Fig. 9. Binary elements plots of Au (ppm) versus Fe (wt.%) based on the TSD for the mapped arsenopyrite grain from the Beaver Dam deposit (Nova Scotia, Canada) and colored by element associations. These diagrams demonstrate that element associations are characterized mainly by stoichiometric values of Au and Fe suggesting they are part of the arsenopyrite grain and not related to late remobilization or inclusions. Note a small group of points shows low Fe and high Fe element association contents which may illustrate remobilization along F2 fractures.

Fig. 10. Binary plot of Ag versus Ni (in ppm) in pyrite grains of both early diagenetic and metamorphic/hydrothermal origin from four sediment-hosted gold deposits reported by Large et al. (2009) - Sukhoi Log (Russia), Bendigo (Australia), Spanish Mountain (Canada) and North Carlin Trend (USA). Based on the distribution of Ag and Au in this diagram, discrimination fields have been defined for early diagenetic, metamorphic/hydrothermal orogenic, and Carlin-type (see Gourcerol et al., 2016a for further discussion).

Fig. 11. Selected multi-element plots of Ag versus Ni (in ppm) plus an additional element for LA ICP-MS TSD for pyrite from the Meadowbank deposit (Nunavut, Canada). Note that additional elemental data are plotted using color codes for various concentrations (i.e., cold to hot) and that these define two elemental groupings, as discussed in the text. The data are also plotted in the context of discriminant fields (see Fig. 10) for different sediment-hosted gold deposits (i.e., diagenetic versus metamorphic/hydrothermal orogenic versus Carlin-type).

Fig. 12. A dendogram plot for agglomerative hierarchical clustering (AHC) statistical analysis of selected elements for TSD for the arsenopyrite grain analyzed from the Beaver Dam deposit (Nova Scotia, Canada). Note the three distinct colors defined the three elemental groupings based on their element affinities.

Fig. 13. Results of multidimensional scaling (MDS) analysis of selected elements for TSD of an arsenopyrite grain from the Beaver Dam deposit (Nova Scotia, Canada). The plots show the relationship between selected elements (A) and their respective Goldschmidt classification (B). Note that Dimension 1 and Dimension 2 have been interpreted, respectively, in the context of fracture controlled enrichment and remobilization due to coupled dissolution/precipitation. Elements are written in color as defined by the dendrograms in the AHC diagram (Fig. 12) whereas field colors correspond to the element association defined from the paragenetic sequence and element map (Figs. 2, 3). For instance, Mo is part of the Primary' event according to the MDS diagram but refers also to F1 element association by the dendrogram as it was slightly remobilized along the fracture set. Note Primary' and Primary refer to the paragenesis in Figure 3.

Fig. 14. Principal component analysis (PCA) diagrams of selected elements based on TSD for an arsenopyrite grain from the Beaver Dam deposit (Nova Scotia, Canada) as a function of PC1 and PC2 (A) and PC1 and PC3 (B). Note the elements are written in the color as defined by the dendrograms in the AHC diagram (Fig. 12) whereas field colors correspond to the element associations defined from the paragenetic sequence and element map (Figs. 2, 3).

Fig. 15. Linear discriminant analysis (LDA) diagrams of selected elements for the TSD for an arsenopyrite grain from the Beaver Dam deposit (Nova Scotia, Canada). Note the elemental associations with Au are discriminated by Au concentration (in ppm) as a function of factors 1 and 2 in plots A and B and factors 1 and 3 in plots C and D. See the text for further details. Also note that F1 refers to the factor explaining 44.92% of the trace element variation and F2 explains 37.07% of the trace element variation. The plots in A) and C) illustrate the variable and vector correlation circles whereas B) and D) represent Au concentration groups as a function of the element vectors (e.g., higher Au concentration associated with Ag and Zn).

Fig. 16. Linear discriminant analysis (LDA) diagrams of selected element associations for TSD for the arsenopyrite grain from the Beaver Dam deposit (Nova Scotia, Canada). Note that the data are discriminated by Au concentration (in ppm) for the function factors 1 and 2 (in plots A and B) and factors 1 and 3 in plots C) and D. In addition, plots A and C illustrate the variable and vector correlation circles whereas plots B and D represent Au concentration groups as a function of the element association vectors (e.g., higher Au concentration associated with factors F1 and F2). Note the element associations are based on the paragenesis sequence (Fig. 3) and “Primary” refers to the Co-Ni association whereas, “Primary’ ” refers to the Mo-Se-Sb element association.

Table 1: LA-ICP-MS Instrumentation and Acquisition Parameters

Laser ablation system	
Instrument	Resonetics RESOlution M-50
Laser type	ArF excimer
Wavelength	193 nm
Pulse duration	20 ns
Repetition rate	5 - 7 Hz
Spot diameter	9 - 48 um
Speed	3 - 18 um/s (typically 1/3 to 1/2 the beam diameter/s)
Energy density	4 - 5 J/cm^2 (mesured)
Carrier gas (He)	650 ml/min
Additional gases	6 ml/min N_2
Primary reference material	NIST610
Secondary reference material(s)	NIST612, BHVO2g, Po725 (some combination thereof)

Mass spectrometer	
Instrument	Thermo X-Series II
Plasma RF power	1440 - 1490 W
Plasma gas flow	730 - 800 ml/min Ar
Isotopes analyzed for D4-A and LC-12-16 maps	^{27}Al, ^{47}Ti, ^{51}V, ^{52}Cr, ^{55}Mn, $^{56, 57}$Fe, ^{59}Co, ^{60}Ni, ^{65}Cu, ^{66}Zn, ^{75}As, ^{82}Se, ^{95}Mo, ^{107}Ag, ^{111}Cd, ^{113}In, ^{118}Sn, ^{121}Sb, ^{182}W, ^{197}Au, ^{208}Pb, ^{209}Bi 10 ms dwell time per analyte total duty cycle of 276 ms
Isotopes analyzed for other traverses and maps	^{33}S, ^{45}Sc, ^{47}Ti, ^{55}Mn, ^{56}Fe, ^{59}Co, ^{60}Ni, ^{65}Cu, ^{66}Zn, ^{75}As, ^{82}Se, ^{95}Mo, ^{101}Ru, ^{103}Rh, ^{105}Pd, ^{107}Ag, ^{111}Cd, ^{115}In, ^{118}Sn, ^{121}Sb, ^{125}Te, ^{182}W, ^{189}Os, ^{193}Ir, ^{195}Pt, ^{197}Au, ^{202}Hg, ^{205}Tl, ^{208}Pb, ^{209}Bi, ^{238}U 10 ms dwell time per analyte except Au, which was 30 ms total duty cycle of 403 ms
ThO^+/Th^+	< 0.6 %
U^+/Th^+	~ 0.95

ThO^+/Th^+ and U^+/Th^+ were determined on NIST612 during instrument tuning

Figure 1

Click here to download Figure Figure 1.tif

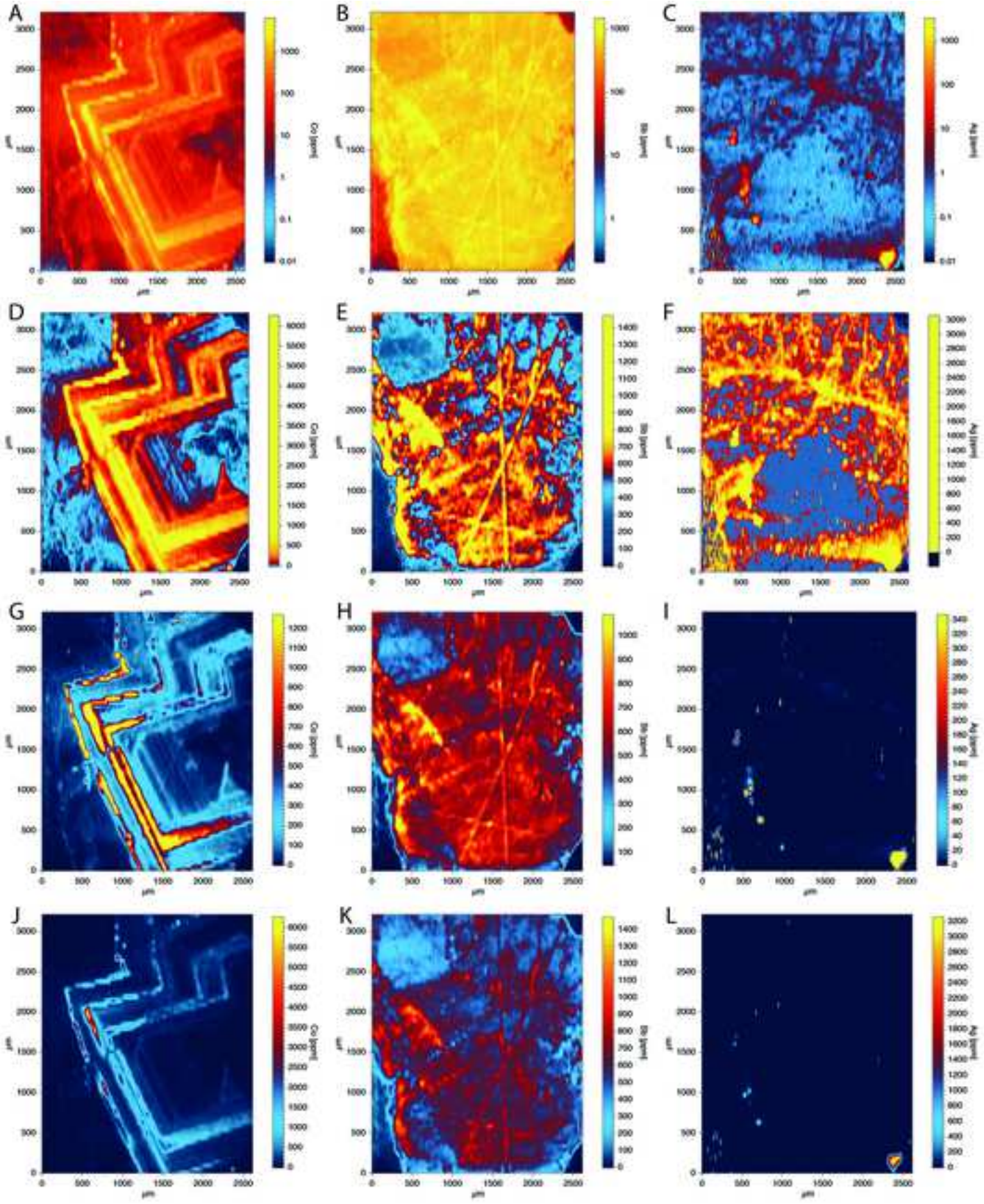

Figure 2

Click here to download Figure Figure 2.tif

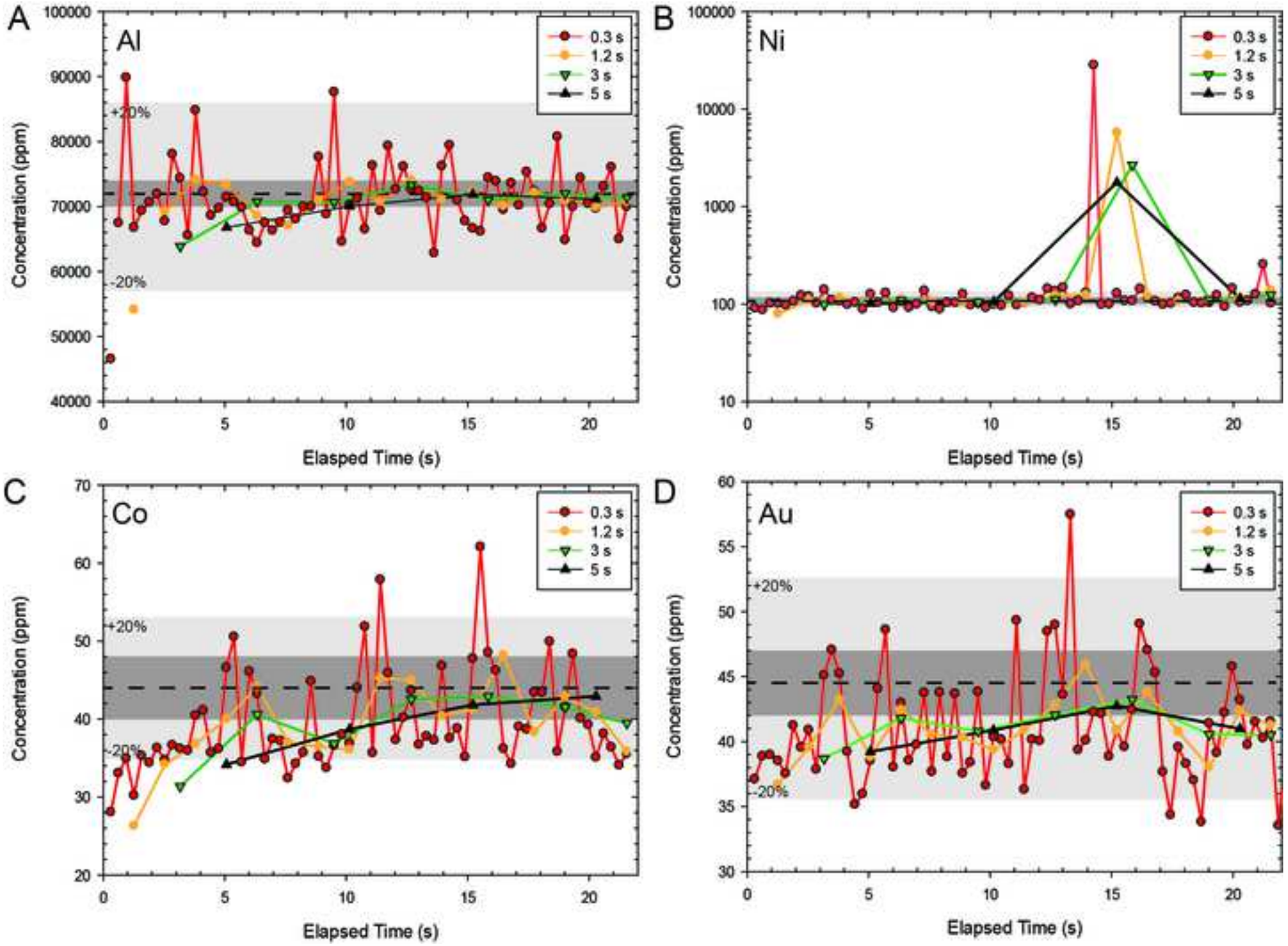

Figure 3

Click here to download Figure Figure 3.tif

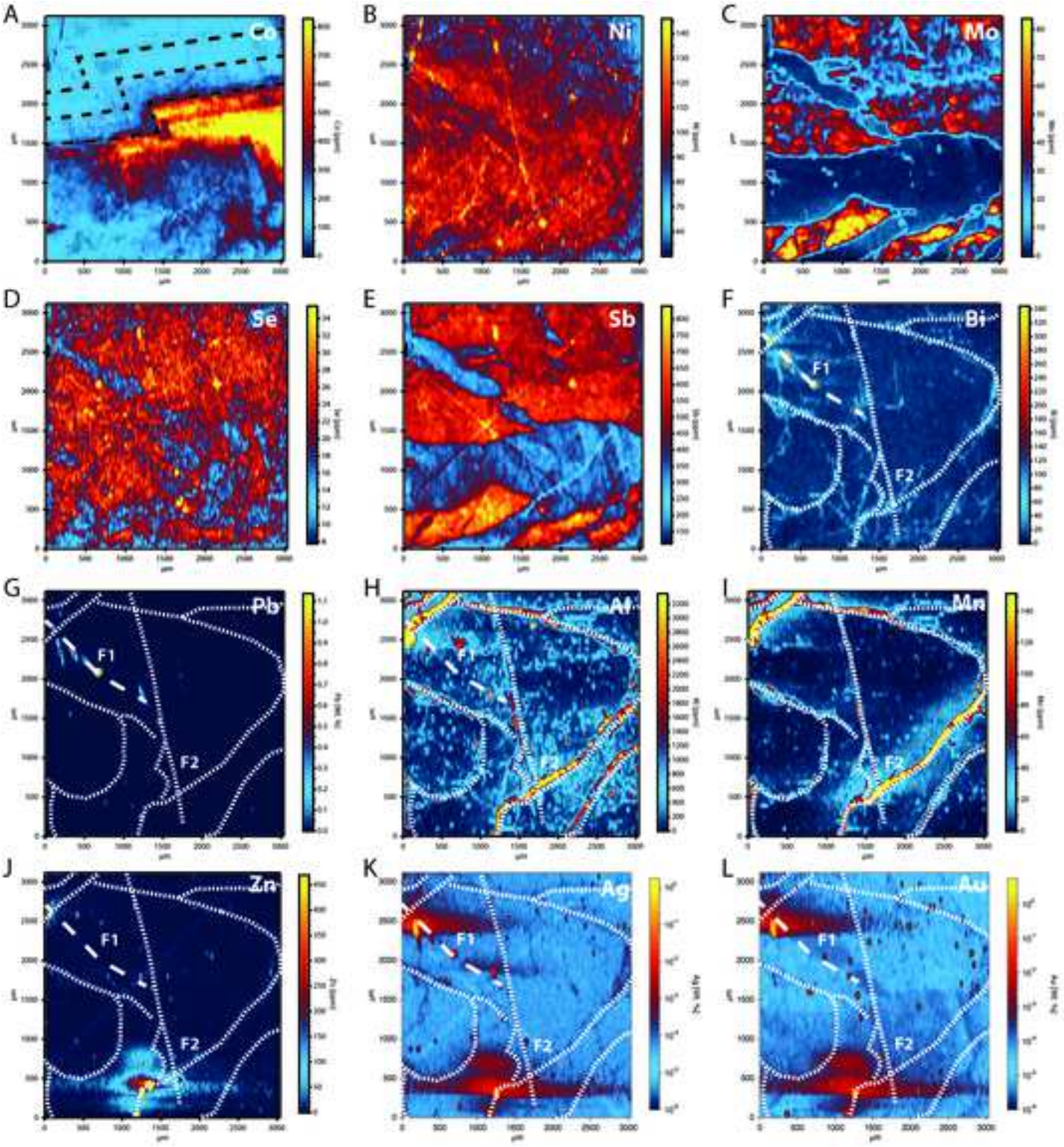

Figure 4

Click here to download Figure Figure 4.tif

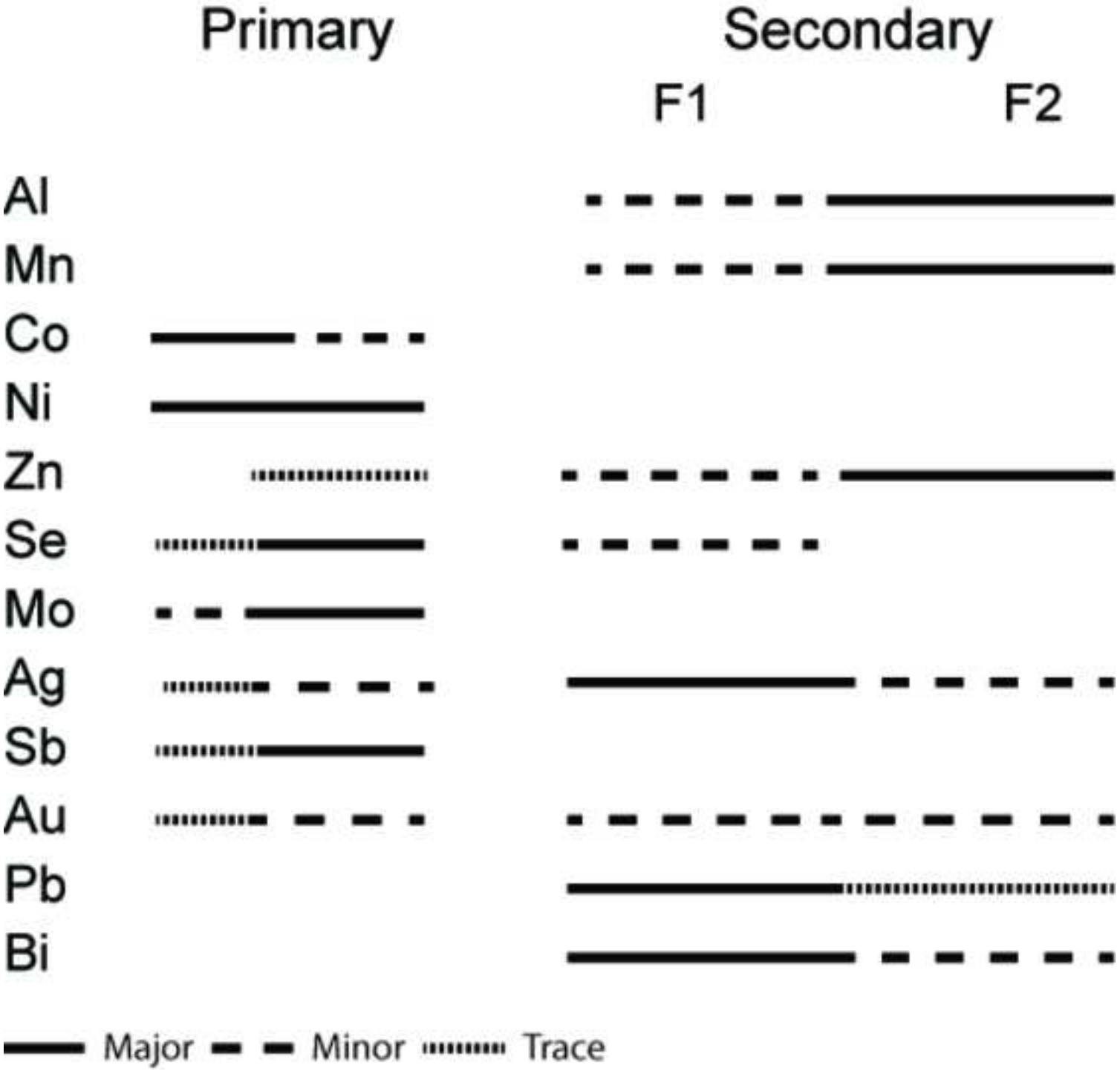

Figure 5

Click here to download Figure Figure 5.tif

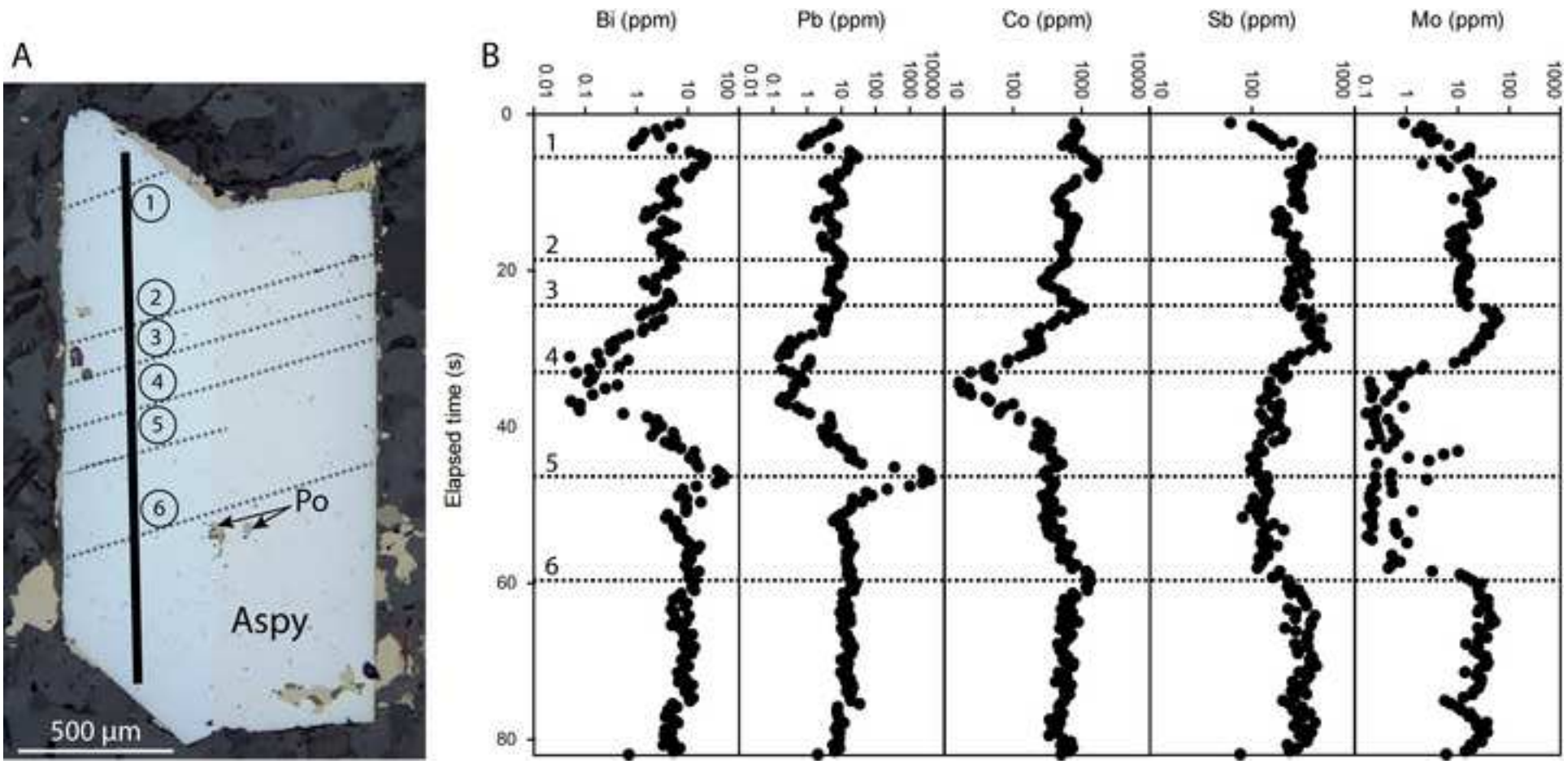

Figure 6

Click here to download Figure Figure 6.tif

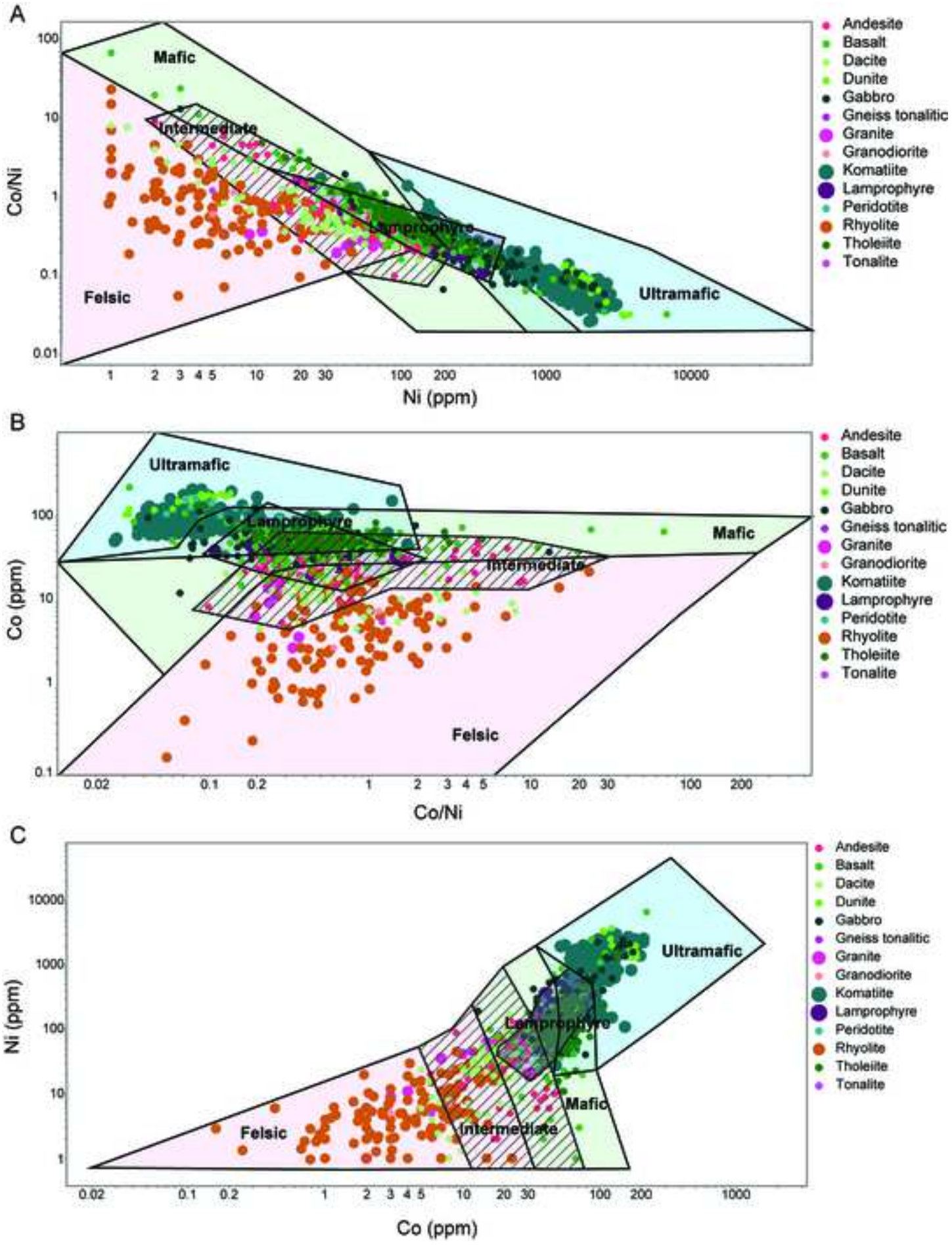

Figure 7

Click here to download Figure Figure 7.tif

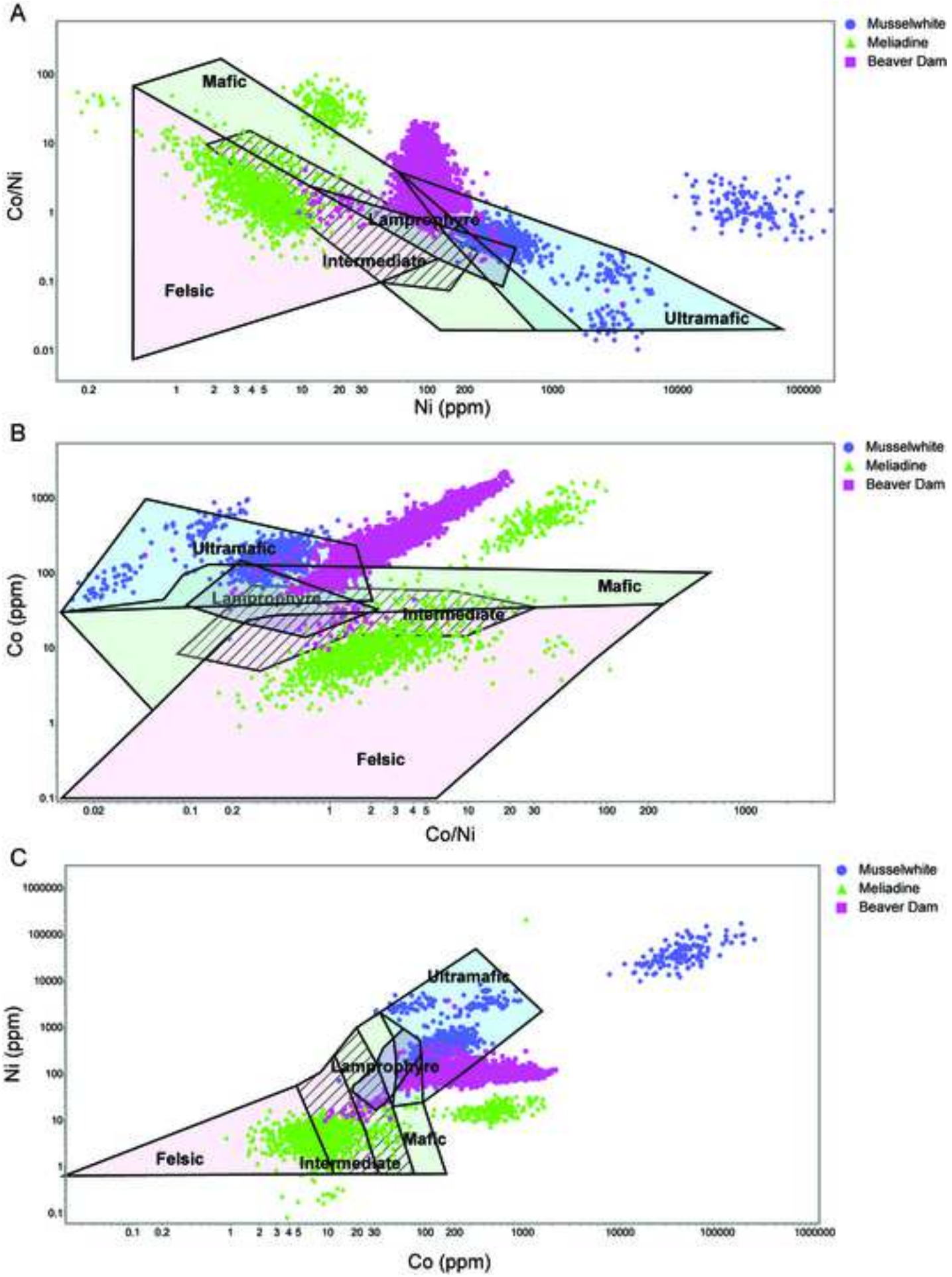

Figure 8

Click here to download Figure Figure 8.tif

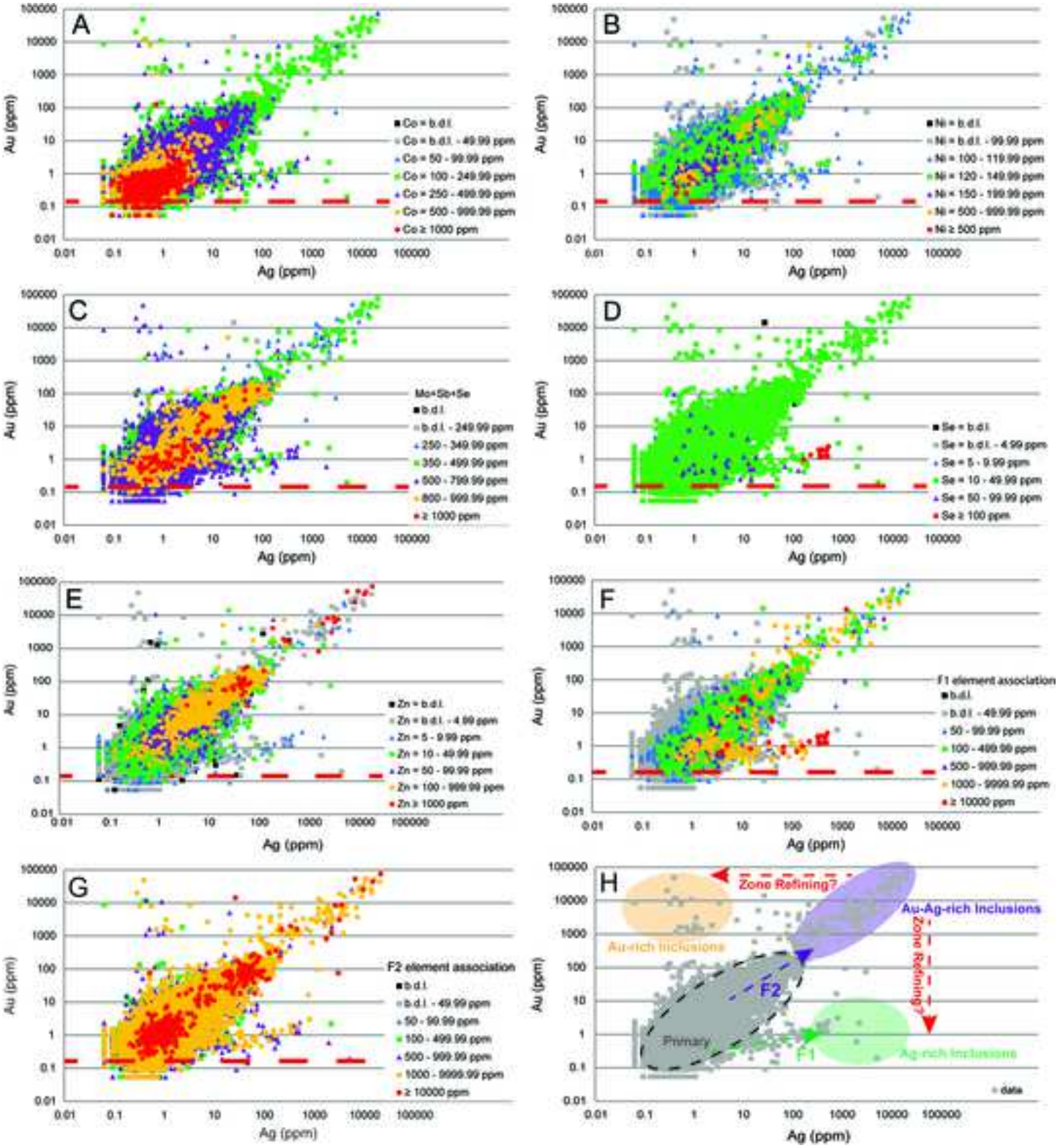

Figure 9

Click here to download Figure Figure 9.tif

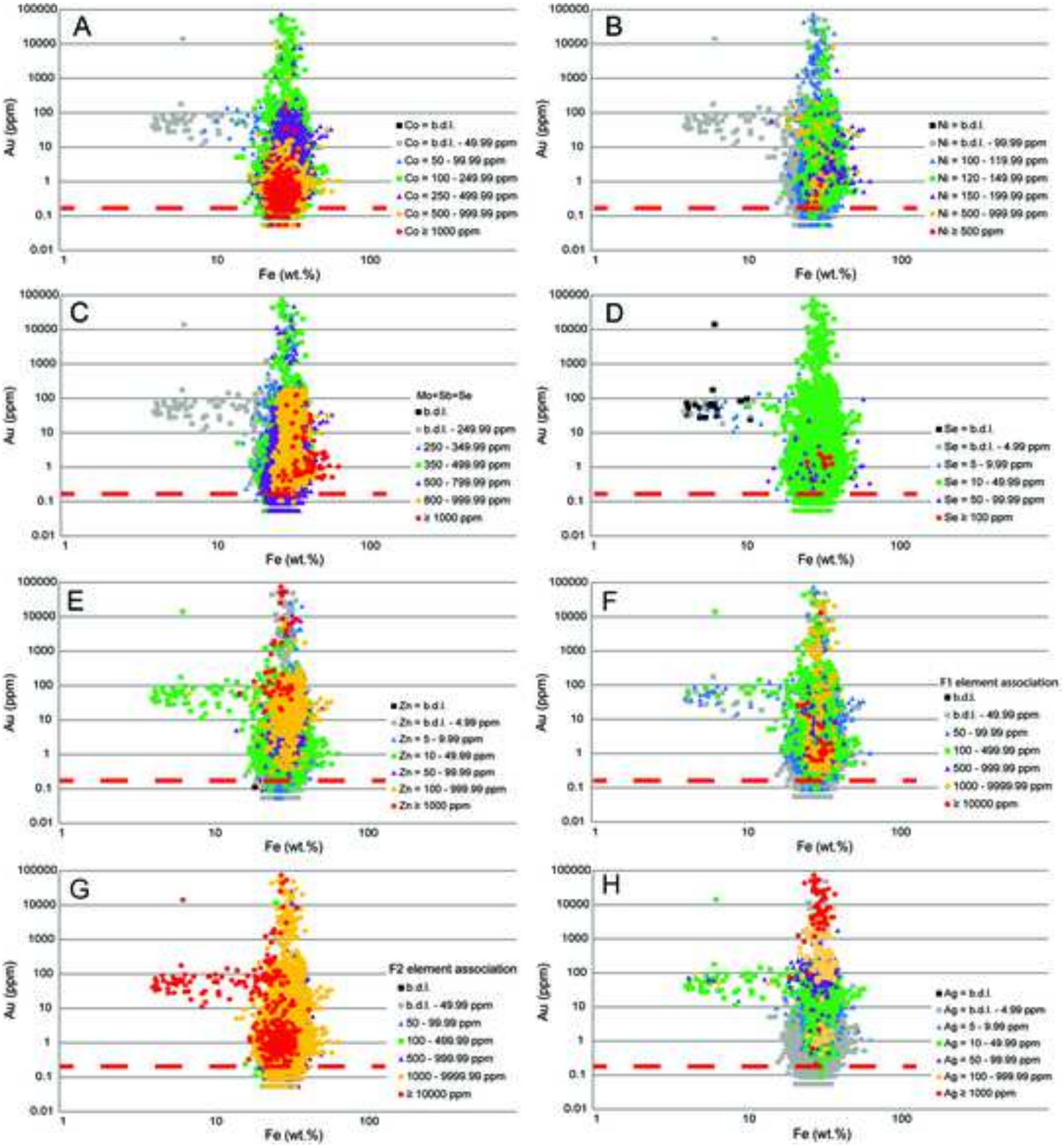

Figure 10

Click here to download Figure Figure 10.tif

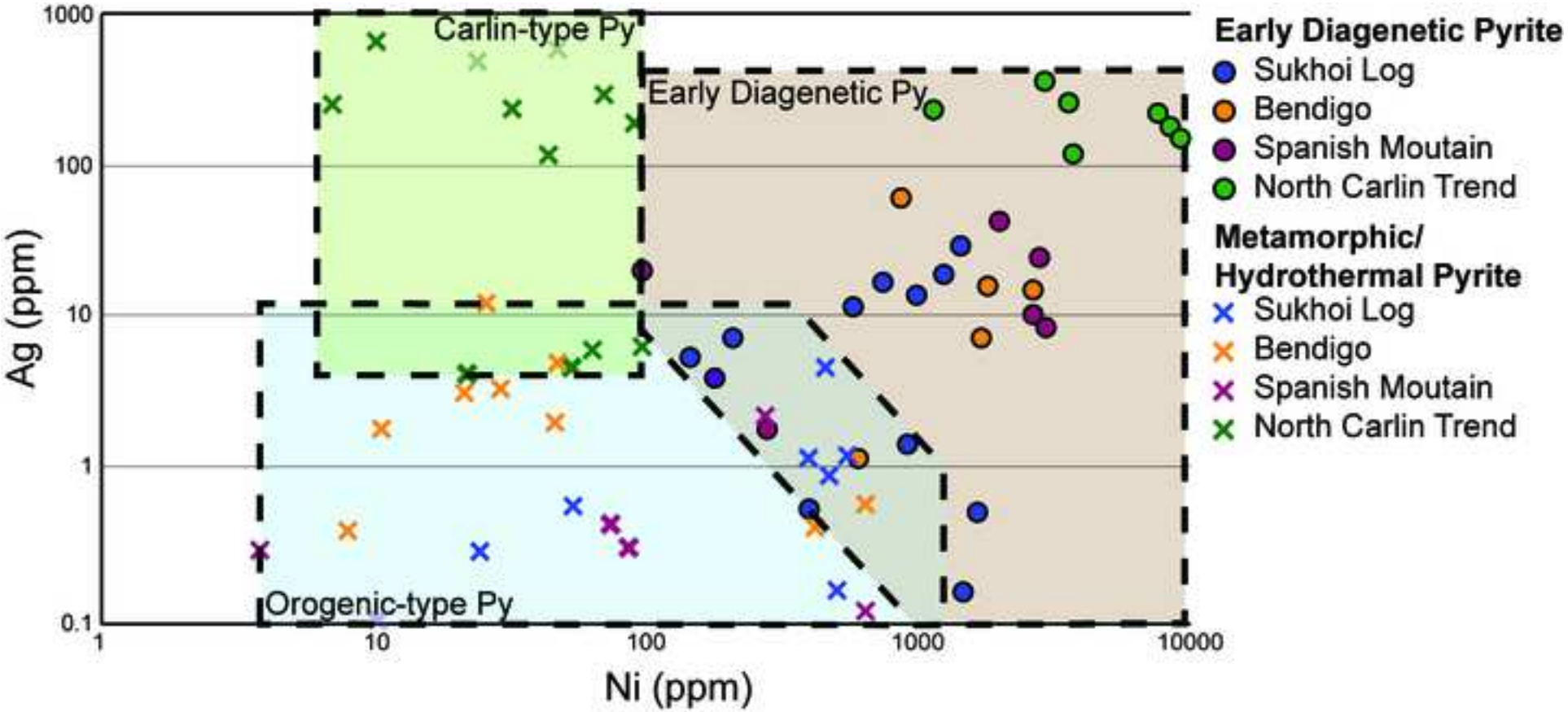

Figure 11

Click here to download Figure Figure 11.tif

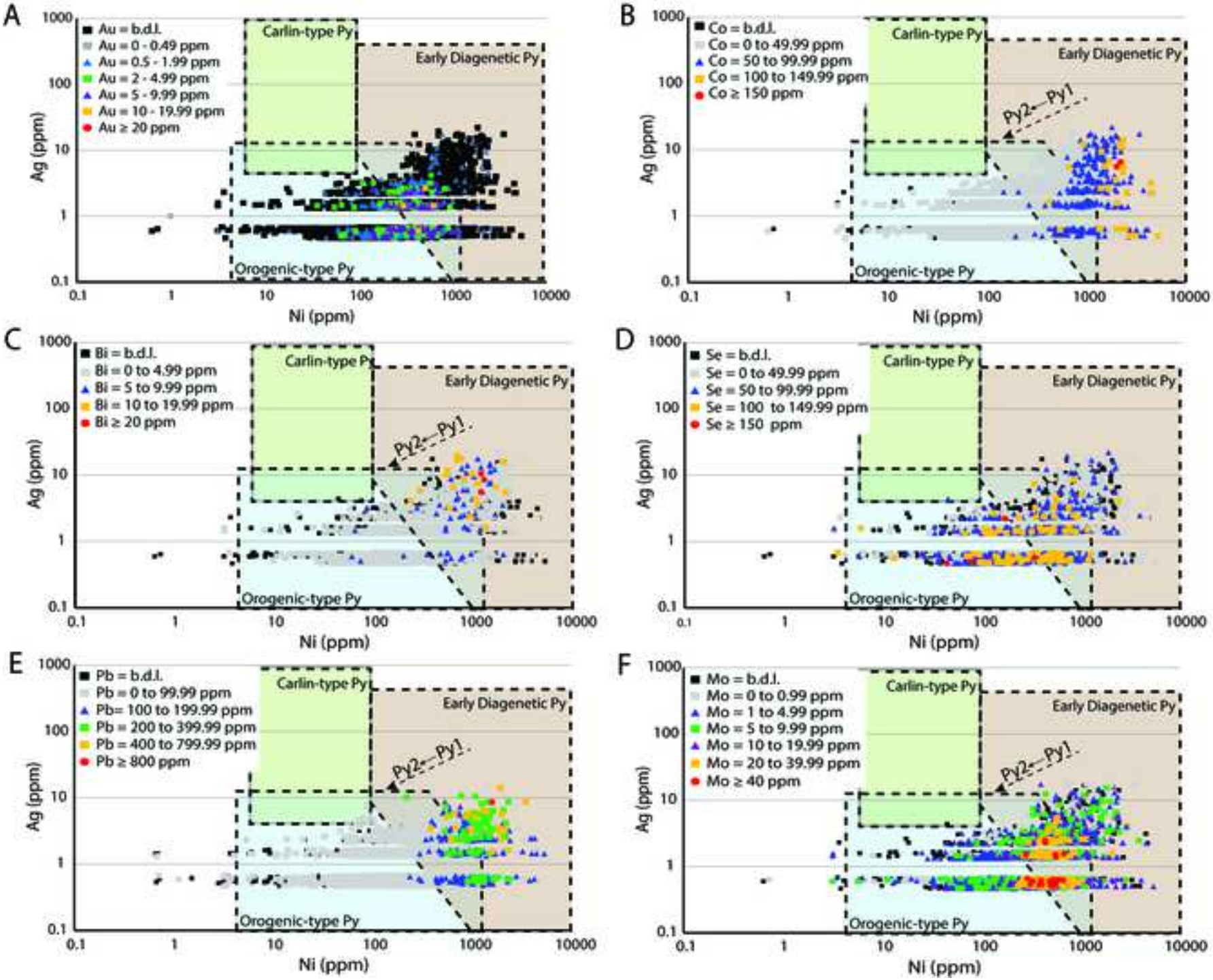

Figure 12

Click here to download Figure Figure 12.tif

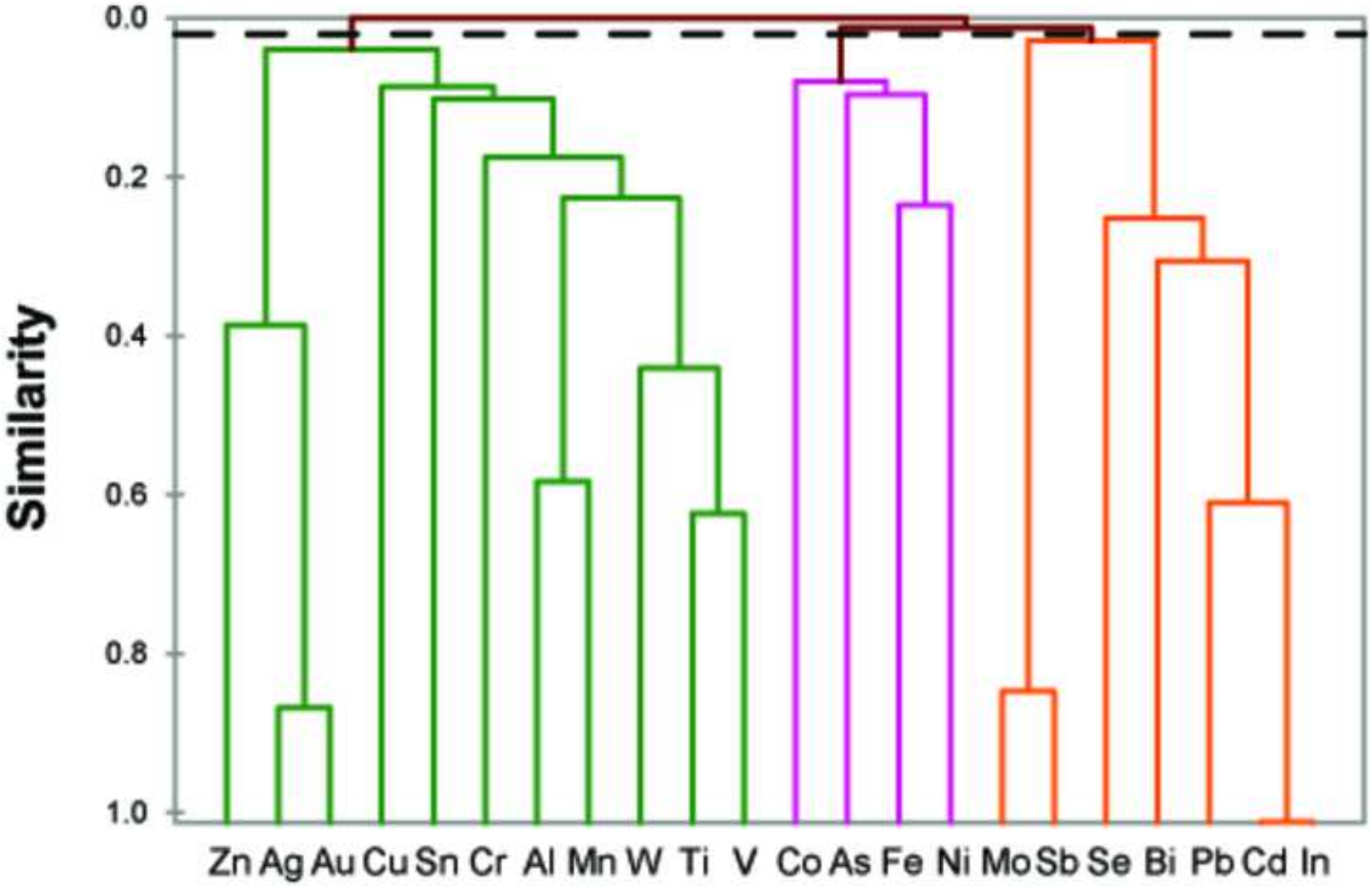

Figure 13

Click here to download Figure Figure 13.tif

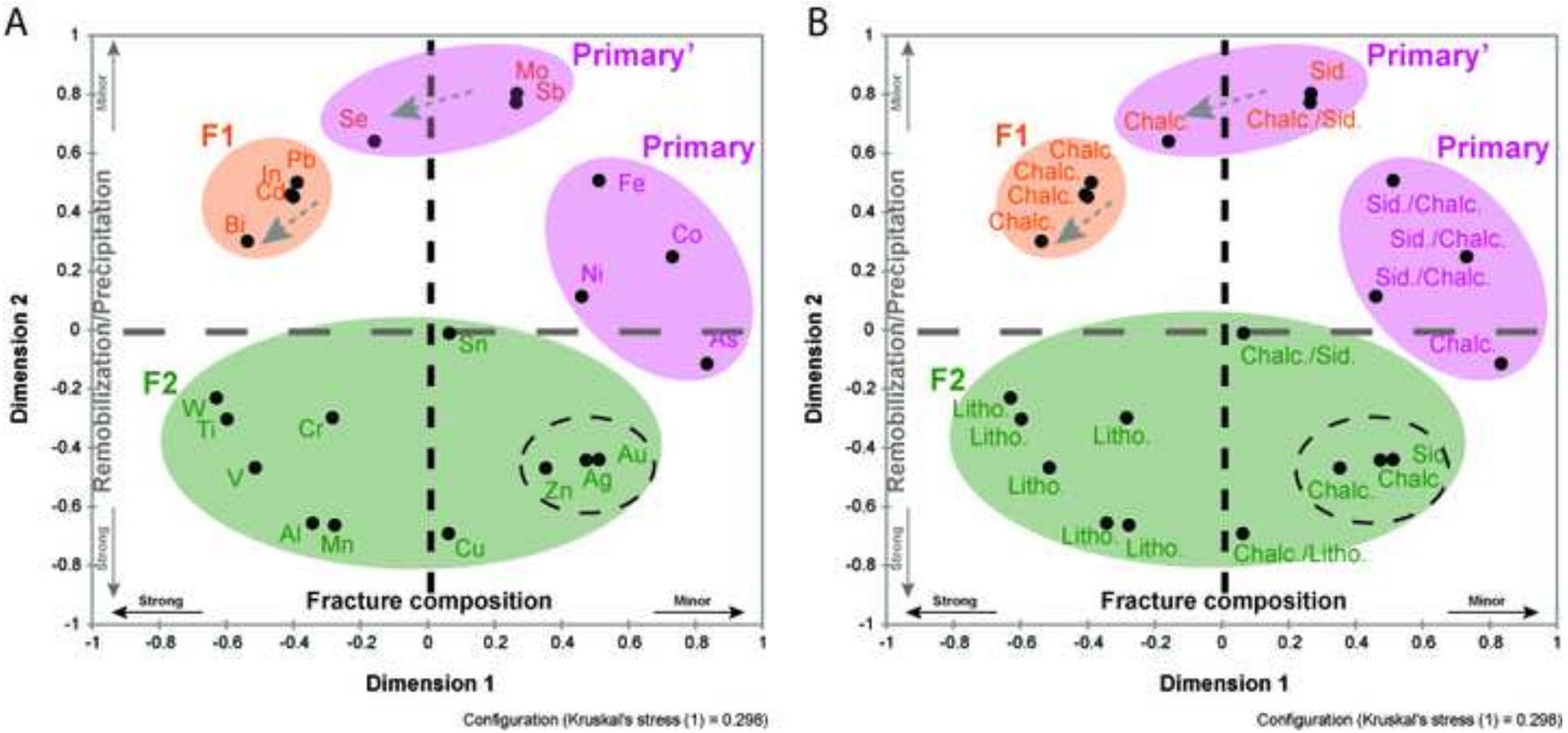

Figure 14

Click here to download Figure Figure 14.tif

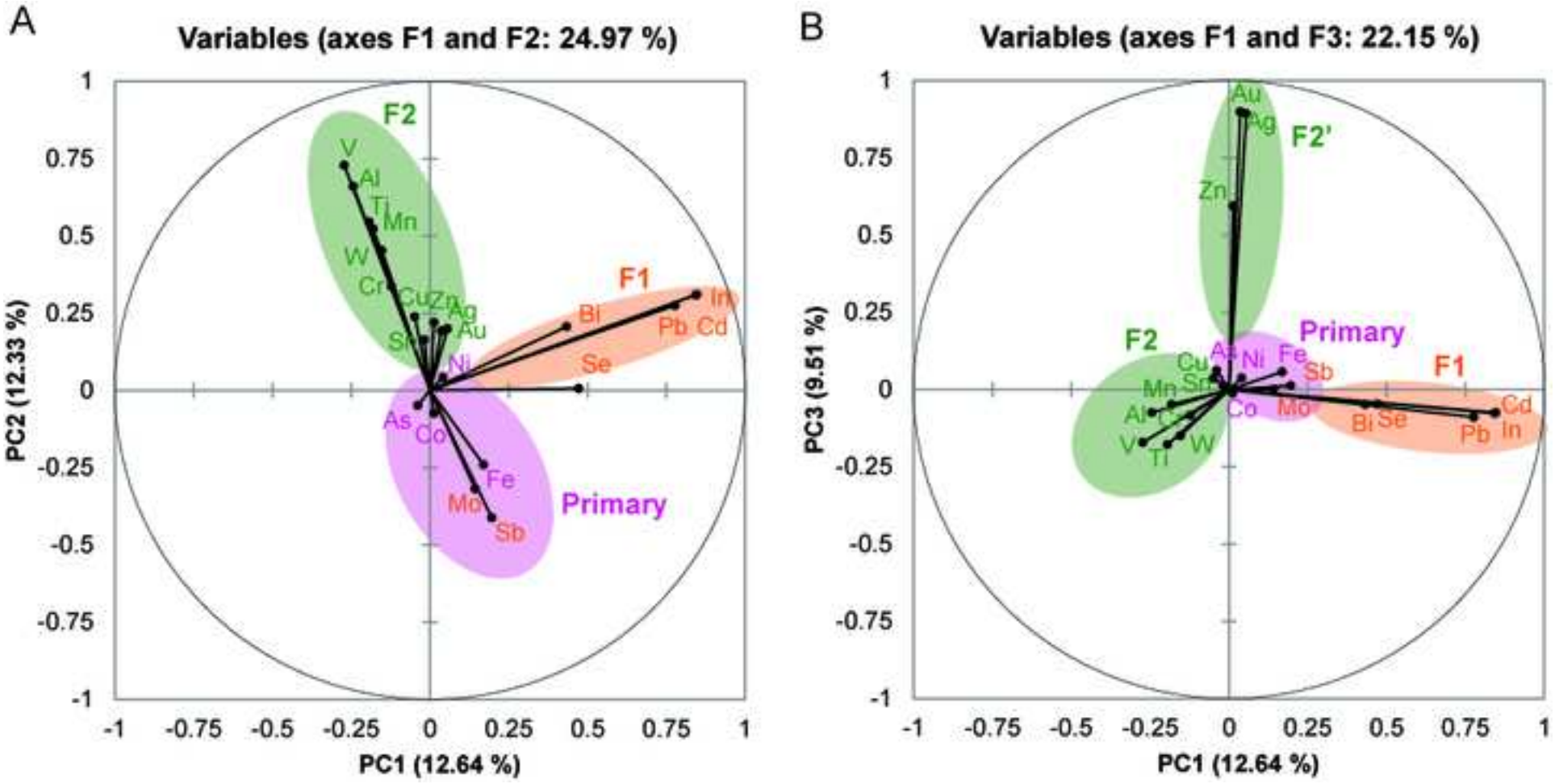

Figure 15

Click here to download Figure Figure 15.tif

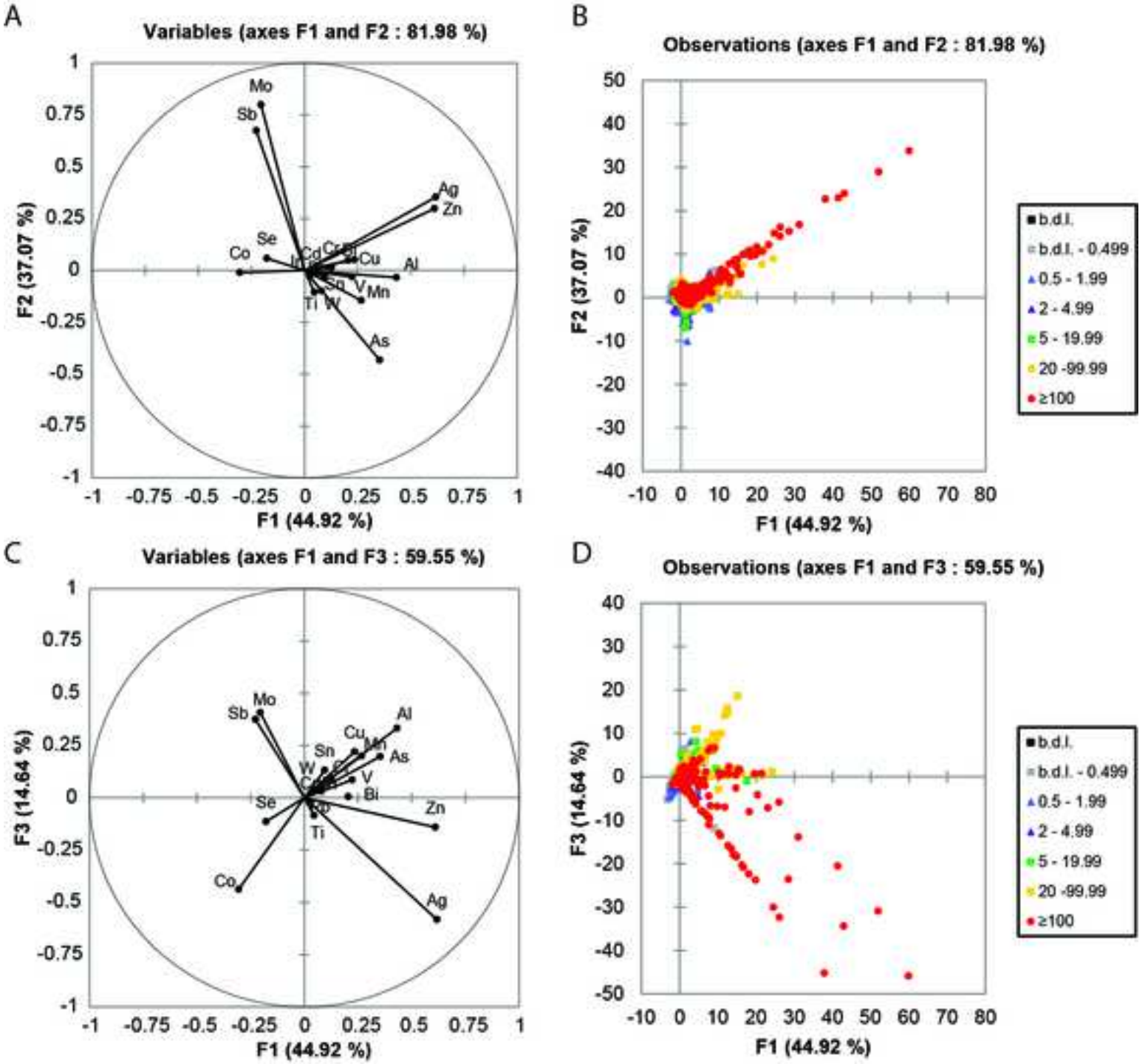

Figure 16

Click here to download Figure Figure 16.tif